Article

Cell Host & Microbe

The NSP4 T492I mutation increases SARS-CoV-2 infectivity by altering non-structural protein cleavage

Graphical abstract

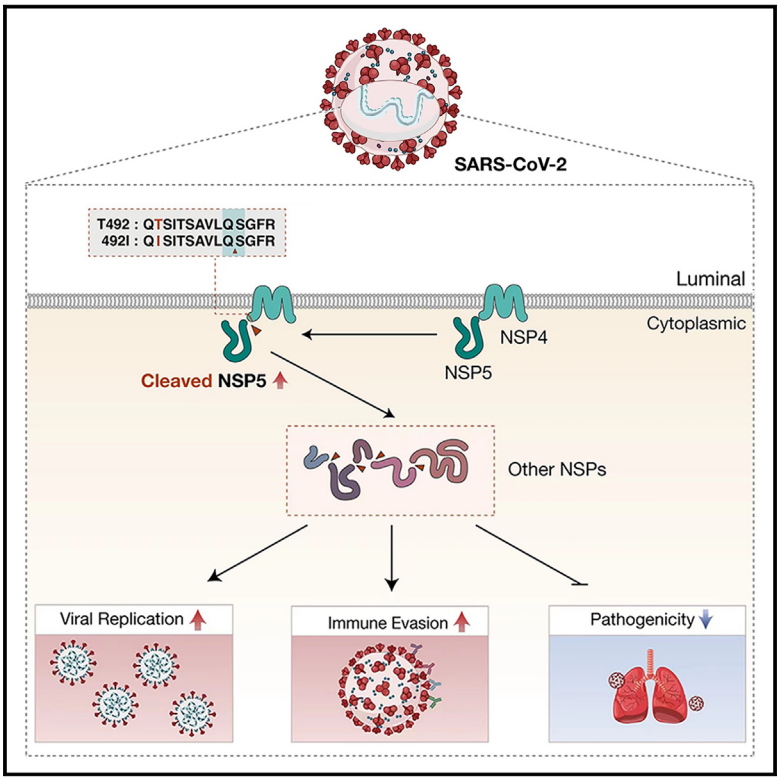

Highlights

- Recent SARS-CoV-2 variants, such as Delta and Omicron, carry a T429I substitution in NSP4
- The NSP4 T492I substitution increases SARS-CoV-2 transmissibility and adaptability
- T492I mutation associates with attenuated pathogenicity of SARS-CoV-2 variants of concern
- T492I mutation alters viral properties by modulating non-structural protein cleavage

Authors

Xiaoyuan Lin, Zhou Sha, Jakob Trimpert, ..., Zhenglin Zhu, Weiwei Xue, Haibo Wu

Correspondence

zhuzl@cqu.edu.cn (Z.Z.), xueww@cqu.edu.cn (W.X.), hbwu023@cqu.edu.cn (H.W.)

In brief

Lin et al. demonstrate that the NSP4 T492I substitution associates with the increased infectivity, transmissibility, and attenuated pathogenicity observed in recent SARS-CoV-2 variants, including Delta and Omicron. Mechanistically, T492I alters non-structural protein cleavage, which changes viral properties. This study highlights the importance of NSP4 in the evolutionary dynamics of SARS-CoV-2.

Lin et al., 2023, Cell Host & Microbe *31*, 1170–1184
July 12, 2023
https://doi.org/10.1016/j.chom.2023.06.002

CellPress

CellPress

Cell Host & Microbe

Article

The NSP4 T492I mutation increases SARS-CoV-2 infectivity by altering non-structural protein cleavage

Xiaoyuan Lin,[1,2,4] Zhou Sha,[1,4] Jakob Trimpert,[2] Dusan Kunec,[2] Chen Jiang,[1] Yan Xiong,[1] Binbin Xu,[3] Zhenglin Zhu,[1,*] Weiwei Xue,[3,*] and Haibo Wu[1,5,*]

[1]School of Life Sciences, Chongqing University, No.55 Daxuecheng South Road, Shapingba, Chongqing 401331, China
[2]Institut für Virologie, Freie Universität Berlin, Robert-von-Ostertag-Straße 7, 14163 Berlin, Germany
[3]School of Pharmaceutical Sciences, Chongqing University, No.55 Daxuecheng South Road, Shapingba, Chongqing 401331, China
[4]These authors contributed equally
[5]Lead contact
*Correspondence: zhuzl@cqu.edu.cn (Z.Z.), xueww@cqu.edu.cn (W.X.), hbwu023@cqu.edu.cn (H.W.)
https://doi.org/10.1016/j.chom.2023.06.002

SUMMARY

The historically dominant SARS-CoV-2 Delta variant and the currently dominant Omicron variants carry a T492I substitution within the non-structural protein 4 (NSP4). Based on *in silico* analyses, we hypothesized that the T492I mutation increases viral transmissibility and adaptability, which we confirmed with competition experiments in hamster and human airway tissue culture models. Furthermore, we showed that the T492I mutation increases the replication capacity and infectiveness of the virus and improves its ability to evade host immune responses. Mechanistically, the T492I mutation increases the cleavage efficiency of the viral main protease NSP5 by enhancing enzyme-substrate binding, which increases production of nearly all non-structural proteins processed by NSP5. Importantly, the T492I mutation suppresses viral-RNA-associated chemokine production in monocytic macrophages, which may contribute to the attenuated pathogenicity of Omicron variants. Our results highlight the importance of NSP4 adaptation in the evolutionary dynamics of SARS-CoV-2.

INTRODUCTION

Severe acute respiratory syndrome coronavirus 2 (SARS-CoV-2) has triggered a global public health crisis since 2019.[1,2] The virus has a moderate mutation rate[3–5] but is in a rapid evolution due to the large number of human infections. Genomic variations and the birth of adaptive mutations enabled the rapid spread of several distinct variants of concern (VOCs).[6–8] The S mutation N501Y[9–12] and the nucleocapsid (N) mutation R203K/G204R[13] play an essential role in the increased infectivity and transmissibility of VOC Alpha, a historical predominant lineage in the first half of 2021. Another S mutation, L452R, was demonstrated to increase infectivity, transmissibility, and resistance to neutralization of VOC Delta, which replaced Alpha as the dominant lineage in the second half of 2021.[14,15] The present ongoing VOC Omicron contains a strikingly high number of mutations,[16] especially in the S protein. These spike adaptations in Omicron allow SARS-CoV-2 variants to dominate the current pandemic.[17] Functional analyses of these important mutations provide clues to the rising of VOCs and the evolutionary trend of SARS-CoV-2, enrich the understanding of molecular and cellular mechanisms of SARS-CoV-2 infection, and guide the development of effective intervention strategies.

Previous work mainly focused on SARS-CoV-2 spike mutations, because the S protein mediates the receptor recognition and fusion processes and is the main target for the development of vaccines and neutralizing antibodies.[18,19] Non-structural proteins (NSPs) have been studied far less than S protein, although NSPs account for more than 70% of the SARS-CoV-2 genome. NSPs constitute the viral replication and transcription complex (RTC),[20] interact with host proteins during the early coronavirus replication cycle, and initiate the biogenesis of replication organelles.[21–23] NSPs have also been reported to be associated with coronavirus pathogenicity,[24–27] and mutations on NSPs may lead to attenuated virulence of Omicron compared with previous lineages.[28] Recently, Chen et al. reported that the spike and NSP6 mutations determine the attenuation of SARS-CoV-2 Omicron variants.[29] In addition, NSP4 is involved in the formation of double-membrane vesicles (DMVs) closely associated with viral replication[30] and, together with NSP3 and NSP6, redirects host inner membranes into replicating organelles.[31,32] Meanwhile, NSP4 induces extensive mitochondrial structural changes, the formation of outer membrane macropores, and the release of mitochondrial-DNA-loaded inner membrane vesicles.[33] Furthermore, NSP4 is known as a strong predictor of mortality in patients with severe COVID-19.[34,35] The functional importance

CellPress

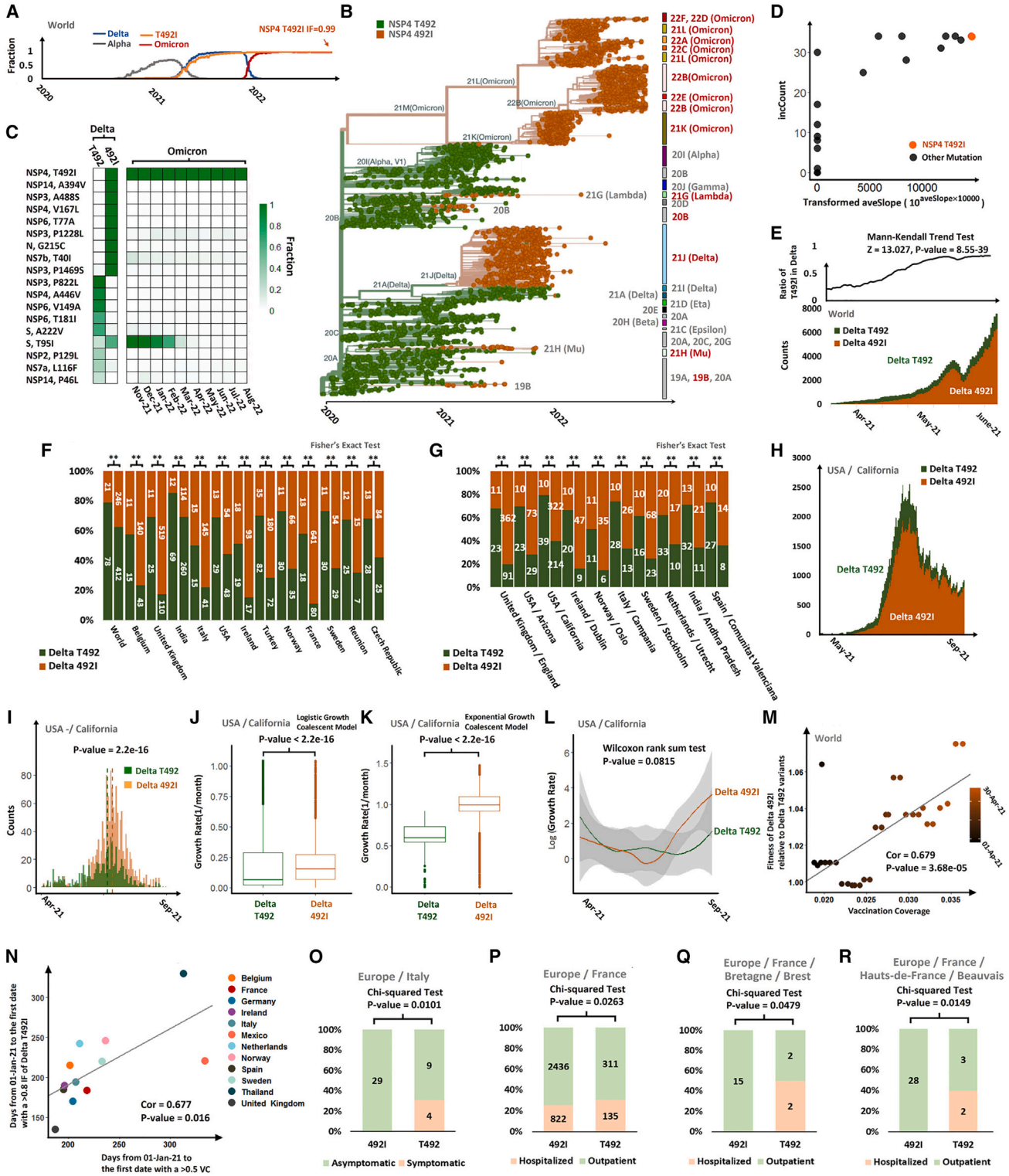

Figure 1. Epidemiological assessment of the impact of NSP4 T492I on the characteristics of SARS-CoV-2

(A) IF changes of T492I and three VOCs (Alpha, Delta, and Omicron) from 2020 to 2022.

(B) A phylogenetic tree of SARS-CoV-2 strains showing the rapid spread of T492I and associated VOCs, marked in red. The phylogenetic tree was acquired from NextStrain and curated.

(C) A heatmap showing the fractions of 18 mutations in Delta 492I, Delta T492, and Omicron variants. The values in the columns Delta 492I and Delta T492 are 6-month median fractions (from April to September in 2021), and those in the Omicron columns are 1-month median fractions.

(legend continued on next page)

of NSP4 suggests that accumulative mutations in this protein may contribute significantly to the phenotypic changes of SARS-CoV-2 along its evolutionary history.

In this study, we targeted the NSP4 mutation T492I, which was shared by the Delta dominant sub-variant (21J) and all Omicron sub-variants. Evolutionary tracks of T492I showed an increase in the incidence frequency (IF) of T492I since January 2021, rapid spread, and then fixation in the worldwide pandemic to date. Comprehensive epidemiological and evolutionary analyses revealed evidence suggesting a transmission advantage, an association with immune evasion, and an attenuation in virulence of T492I. Through experimental studies conducted in cell lines, hamsters, and human airway tissue models, we identified and validated increased infectivity and fitness of the 492I variant. Further, we found a decreased sensitivity of virus carrying the 492I mutation toward the sera of hamsters infected with wild-type SARS-CoV-2 virus, suggesting an enhanced immune evasion capability. Moreover, we observed a decrease in the severity of 492I virus-infected hamster lung tissues. In summary, our results suggest that NSP4 T492I substitution plays an essential role in the rapid spread and enhanced immune evasion capability of SARS-CoV-2 VOCs, from Delta to Omicron.

RESULTS

Evolutionary trajectory of the NSP4 T492I mutation

Based on the genomic sequences of VOCs and the information provided by NextStrain[36] and the Global Initiative on Sharing Avian Influenza Data (GISAID),[37] we tracked the historical evolutionary trajectory of the T492I (C10029T) mutation in the nonstructural protein 4 (NSP4). The results showed that T492I initially appeared in early variants (19B and 20B, in the beginning of 2021) and had an increase in IF before the emergence of Delta (Figures 1A and 1B). T492I was shared by Delta, Omicron, Lambda, and Mu (Figure 1B). Delta lineage 21J carried T492I, but the other two Delta lineages, 21A and 21I, did not (Figure 1B). Delta 21J had a higher transmission frequency than Delta 21A+21I and was the dominant strain when Delta reached a nearly fixed frequency (Figures S1A and S1B). Omicron later replaced Delta as the global dominant VOC and the mutation T492I reached an IF of nearly 100% in all Omicron sub-lineages (Figures S1C–S1F). At date of writing, T492I is a fixed NSP4 mutation all over the world (Figures 1A and 1B). These suggest a potentially important contribution of T492I to the fitness and transmission of SARS-CoV-2.

In silico prediction of the T492I impact on SARS-CoV-2 properties

Since both T492 and 492I are carried by multiple VOC lineages (Figure S1G), the individual effect of T492I may be overshadowed by other mutations. In order to increase sensitivity, we compared the IF of mutations within Delta variants (Delta T492 and Delta 492I, "IF_Change.xls" in Mendeley data), because of the low IF of 492I in Alpha and the low IF of T492 in Omicron (Figures S1C and S1G). Of the 18 mutations (IF > 0.1) that differentiated Delta T492 and Delta 492I, T492I was the only one that remained present in all Omicron variants (Figures 1C and S1H). Further, we performed a two-locus combination test for the 18 mutations within Delta strains (see also STAR Methods). The results showed that all combinations with 492I had higher growth rates than those with T492, and that the growth rates of T492I mutation in the relevant combinations were higher than that of other mutations (Figure 1D; Table S1). These data suggest a potentially dominant contribution of T492I to the increase in IF of Delta 492I relative to Delta T492. Therefore, we evaluated the impact of T492I by comparing Delta T492 and Delta 492I.

Following previous efforts,[6,13] we performed Fisher's exact test (Fisher's test) of the Delta 492I fractions of a pair of Delta lineages on the potential onset and the day 1 month later (see also STAR Methods). We also performed Mann-Kendall trend test (MK test) and isotonic regression analysis (IR test) within a 3-month time window after the global onset. To avoid bias toward specific geographic regions and spatiotemporal variation in viral genome sequencing and data deposition, statistics were performed at three geographic scales: world, country, and regional subdivision. The global IF increase of 492I in Delta variants started at the beginning of April 2021 (Figures 1B and 1E) and the increase was significant in Fisher's test, MK test,

(D) A scatter diagram showing the incCount and the transformed aveSlope ($10^{aveSlope * 10,000}$) of the 18 mutations. The mathematic transformation of aveSlope is for the convenience of comparison. The dots for T492I are in orange, and the dots for other mutations are in black. See STAR Methods for the details of incCount and aveSlope.
(E) The upper panel shows the changes in the ratio of the Delta T492I with the result of the Mann-Kendall trend test listed at the top. The lower panel shows the weekly running counts of the Delta T492 and Delta 492I variants from April 2021 to June 2021.
(F) Comparison of the fractions of the Delta T492 and Delta 492I variants at two time points separated by a gap of 1 month in different countries, corresponding to Table S2. "**" denotes significance in Fisher's test. The counts of identified samples are marked within bars.
(G) Comparison between Delta T492 and Delta 492I variants in different regional subdivisions.
(H) Comparison of weekly running counts between Delta T492 and Delta 492I variants in USA-California.
(I) Counts of California Delta T492 and Delta 492I clusters when first detected and over time. Two dotted lines denote the median of Delta T492 (green) and Delta 492I (orange), respectively.
(J–L) Comparison of phylodynamic growth rates between Delta T492 and Delta 492I variants collect in USA-California from April 2021 to September 2021.
(J) and (K) are comparison of the growth rates across states in a logistic growth coalescent model and an exponential growth coalescent model, respectively.
(L) Comparison of growth rates (logged in the plot) over time simulated in the skygrowth coalescent model.
(M) Correlation analysis results between the predicted global fitness of Delta 492I relative to Delta T492 variants (y axis) and VC (x axis) in April. The color of the dots corresponds to the date.
(N) Correlation analysis results between the days from 1 January 2021 to the date when Delta T492I reaches a >0.8 IF and the days from 1 January 2021 to the date when VC reaches 0.5 in different countries, which are differentiated by different colors.
(O–R) Prediction of the clinical outcomes of Delta T492 and Delta 492I variants. Collection sites are listed at the top of the figures. y axis shows the ratios between lineages with opposite patient statuses. Lineage numbers are provided. The significance of changes in ratios were tested by chi-squared test.
See also Figure S1.

and IR test (Figures 1E and S1I; Tables S2 and S3). In statistics at country and regional subdivision levels, most of the statistically significant samples showed an increase of Delta 492I relative to Delta T492 (Figures 1F–1H and S1J–S1L; Tables S2 and S3). Specifically, all 13 countries that were significant in Fisher's test showed an increase in IF (binomial test, p value 0.00024, Figure 1F; Table S2). Out of the 17 countries with significant differences both in MK test and IR test, 13 had an increase in IF (binomial test, p value 0.0049, Figures S1J and S1K; Table S3). For all the regional subdivision cases with a statistical significance in Fisher's test, 10/10 had an increase in IF (binomial test, p value 0.00195, Figure 1G; Table S2). For all the regional subdivision cases with a statistical significance both in MK test and IR test, 26/28 had an increase in IF (binomial test, p value 3.032e−6; Table S3). Further, we applied classic population genetic models to evaluate the fitness of Delta 492I relative to Delta T492 in California, USA, with an increased IF of Delta 492I as referred above (Figures 1H and S1L; Tables S2 and S3). We compared phylogenetic clusters of Delta T492 and Delta 492I variants collected in this regional subdivision in a 6-month interval (from April 2021 to September 2021) following the onset (see STAR Methods for details), and the results indicated a higher transmission rate of Delta 492I relative to Delta T492 (Figures S1M–S1O; see also STAR Methods). Simulation with a logistic coalescent model, an exponential growth coalescent model, and a skygrowth coalescent model all showed that the growth rates of Delta 492I variants were higher than those of Delta T492I variants (Figures 1J–1L, S1P, and S1Q). The increased growth rate of Delta 492I relative to Delta T492 suggests a potential increase in the fitness of 492I over T492.

We calculated the predicted fitness of Delta 492I relative to Delta T492 and compared the relative fitness and the global vaccination coverage (VC) records in 2021 to evaluate the impact of T492I on the immune evasion of SARS-CoV-2. The results showed a global increase in predicted relative fitness in the month following the onset (Figure S1R) and this increase was correlated with a global increase in VCs (Figure 1M; see also STAR Methods). Moreover, we observed a correlation between the date a country first reached a high IF and the date the VC of the country first increased to a certain degree (Figure 1N; Table S4; see also STAR Methods), suggesting that an earlier vaccinated country mostly reached a high IF of Delta T492I at an earlier time. These imply a potential association between T492I and immune evasion capacity.

Finally, we predicted the potential clinical outcome of T492I by performing statistical analyses of sequenced strains with patient information ("Clinical_Info.xls" in Mendeley data, from GISAID). Vaccinated cases were excluded from the analysis to avoid potential distraction. We compared the ratios of opposite disease state pairs between Delta T492 and Delta 492I variants collected in a 6-month interval after the onset of Delta. The comparisons were at two geographic scales, country, and region subdivision, to reduce the potential bias due to the differences between countries/regions. Despite the limited amount of data, we found that Delta 492I variants caused a lower ratio of severe illness than Delta T492 variants in samples from two countries and two region-subdivisions (Figures 1O–1R). These suggest that T491I may have attenuated the virulence of SARS-CoV-2.

The T492I mutation endows SARS-CoV-2 with higher competitiveness and infectivity

Based on the *in silico* analysis, we evaluated the impact of NSP4 T492I mutation on SARS-CoV-2 by experiments. We constructed a 492I variant based on the USA_WA1/2020 SARS-CoV-2 sequence (GenBank: MT020880) and conducted competition experiments using a Syrian hamster model as previously described.[13,38,39] The results showed that a higher 492I to T492 ratio was observed at 3 and 5 days post infection (dpi), indicating a sustained advantage of 492I virus over T492 virus in hamsters (Figures 2A and S2A). Similar competition experiments were conducted in a human airway tissue culture model. We found that, when airway tissues were infected with control and 492I virus at a ratio of 1:1, the ratio of 492I variant to T492 virus increased from 1 to 5 dpi (Figure 2B). After infection of airway tissues with control virus and 492I variant in a 3:1 or 9:1 ratio, 492I variant rapidly overcame the initial deficit and showed an advantage over the control virus (Figures 2C and 2D). These data indicate that 492I variant could rapidly outcompete the T492 virus in human airway tissues.

Next, we tested the replication and infectivity of 492I variant in Vero E6 monkey kidney cell line and Calu-3 human lung epithelial cell line. The results showed that 492I variant replicated with higher extracellular viral RNA (1.32- to 4.76-fold) than T492 virus at 24 and 36 h post infection (hpi) (Figure S2B). The infectivity of virus was measured by PFU titers and viral subgenomic RNA (E sgRNA) loads. As a result, there were no significant differences in PFU titers (1.25- to 1.70-fold) and E sgRNA loads (1.12- to 1.58-fold) between 492I variant and T492 virus in Vero E6 cells (Figures S2C and S2D); however, in Calu-3 cells, 492I virus produced significantly higher extracellular viral RNA (1.45- to 11.31-fold) than the control (Figure S2E), and similar trends in infectious titers (1.22- to 3.37-fold) and E sgRNA loads (0.97- to 3.68-fold) were observed (Figures S2F and S2G). In line with these results, we found that extracellular viral RNA (1.85- to 14.52-fold), PFU titres (1.73- to 5.34-fold), and viral E sgRNA loads (1.68- to 4.29-fold) of 492I variant were significantly higher than those of T492 virus in human airway tissue cultures (Figures 2E–2G). Furthermore, replication and infectivity tests were conducted using a hamster model. As a result, although hamsters infected with different viruses showed similar weight loss during the infection (Figure S2H), viral RNA (Figures 2H and S2I), infectious titers (Figures 2I and S2J), and E sgRNA loads (Figures 2J and S2K) in nasal wash and trachea samples from hamsters infected with 492I variant at 3 and 5 dpi were significantly higher than in controls. Taken together, these results indicate that NSP4 T492I mutation enhances viral replication and infectivity of SARS-CoV-2.

The T492I mutation increases the cleavage efficiency of NSP5

We explored strategies by which the T492I mutation affected viral properties. SARS-CoV-2 gene order is similar to that of other known coronaviruses, with the first two open reading frames (Orf1a and Orf1b) encoding all NSPs.[20] NSP4 protein is a 500-amino acid protein with four predicted transmembrane domains, and T492I mutation is located next to the NSP4|5 cleavage site (also known as the N-terminal autoprocessing site of NSP5) (Figure 3A). NSP5 (M pro or 3CL-pro) is thought to cleave the viral polyprotein at multiple distinct sites, yielding

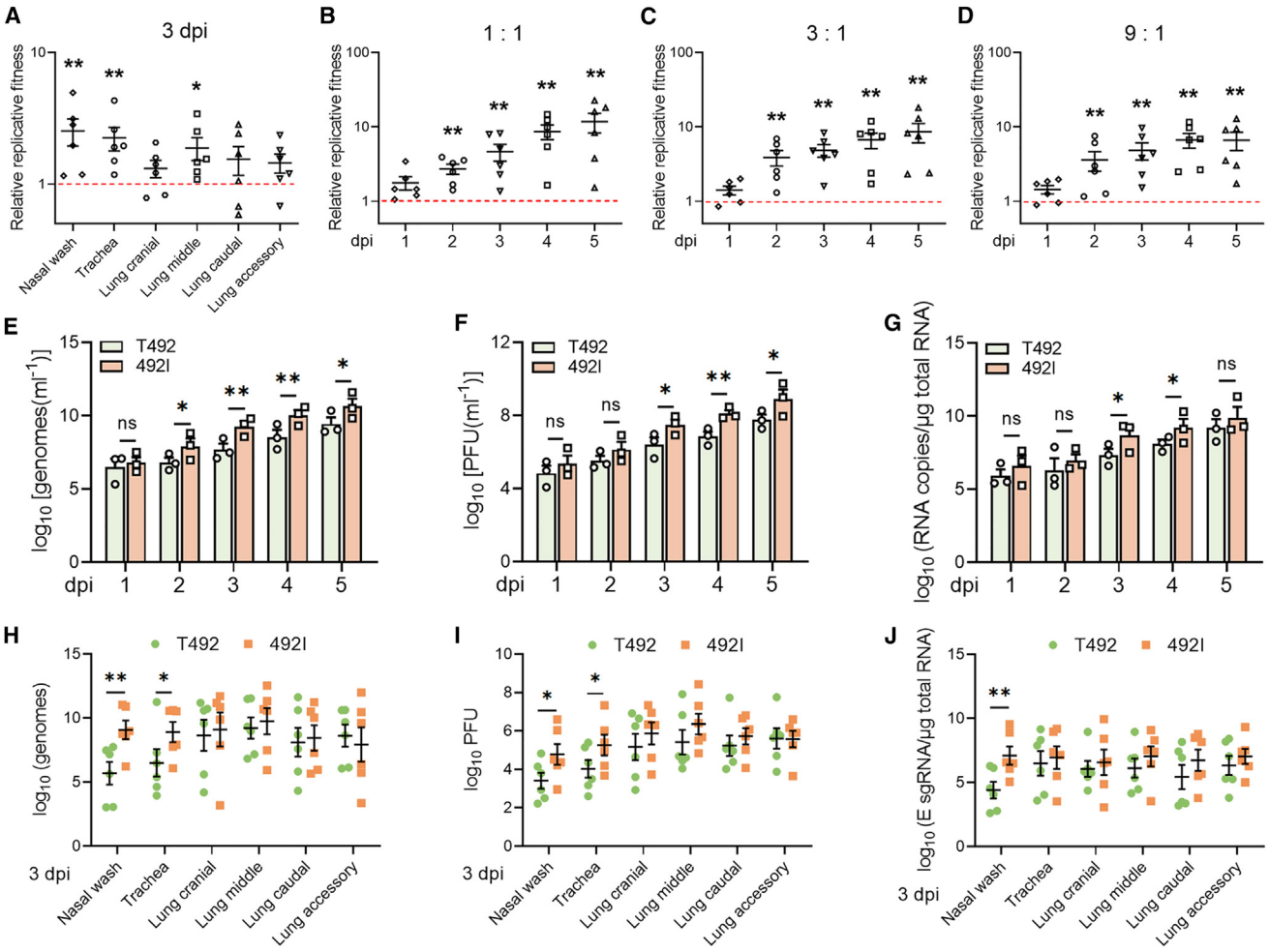

Figure 2. SARS-CoV-2 bearing a T492I mutation has higher competitiveness and infectivity

(A) Hamsters were infected with T492 and 492I virus at a mixture of 1:1. The relative amounts of T492 and 492I viral RNA in nasal wash, trachea and lung samples were detected by RT-PCR and Sanger sequencing at 3 dpi. Log_{10} scale was used for the y axis. Dots represent individual hamsters (n = 6).

(B–D) Mixture of T492 and 492I virus was inoculated into human airway tissue cultures at an initial ratio of 1:1 (B), 1:3 (C), or 1:9 (D) with a MOI of 5. Relative amounts of T492 and 492I viral RNA were detected by quantitative real-time PCR (qRT-PCR) and Sanger sequencing for 5 consecutive days. Log_{10} scale was used for the y axis. Dots represent individual tissue culture (n = 6).

(E–G) T492 or 492I virus was inoculated into human airway tissue cultures at a MOI of 5. Genomic RNA levels (E), PFU titres (F), and E sgRNA loads (G) were detected for 5 consecutive days. Experiments were performed in triplicate.

(H–J) Hamsters were infected with 2×10^4 PFU of T492 or 492I virus. Genomic RNA levels (H), PFU titres (I), and E sgRNA loads (J) in nasal wash, trachea, and lung samples were detected at 3 dpi. Dots represent individual hamsters (n = 6). All data are presented as the mean ± SEM. *p < 0.05, **p < 0.01. Abbreviation: ns, nonsignificant.

See also Figure S2.

NSPs NSP5–NSP16 that support viral replication and disable host defense.[40,41] It has been reported that the amino sequence of the N-terminal autoprocessing site is essential for the cleavage efficiency of NSP5. Inhibition of the NSP5-mediated cleavage prevents NSPs production and results in impaired viral replication.[20,42,43] Based on these, we speculated that T492I mutation might affect the cleavage efficiency of NSP5. To address this hypothesis, we constructed a fusion protein substrate with a linker sequence based on the NSP4|5 cleavage site in-between a 3×FLAG-His tag and the full-length GFP (Figure 3B). In this gel-based cleavage assay, we found that the cleavage efficiency of NSP5 on T492I linker substrate was higher than that on control linker substrate and that cleavage was observed as early as 30 min in T492I group (Figure 3C). These data imply that the T492I mutation enhances the cleavage efficiency of NSP5.

To compare the enzyme activity of NSP5 on different substrates, we performed fluorescence resonance energy transfer (FRET)-based assays using a synthesized 14-amino-acid-long peptide substrates based on the NSP4|5 cleavage site. The FRET peptide contains a fluorophore (2-aminobenzoyl [Abz]) at its N terminus and a quencher (N-Tyrosine) at its C terminus. NSP5 cleaves the substrate and releases fluorophore from the proximity of quencher, resulting in an increase in fluorescent signal (Figure 3D). Using the FRET peptides, we determined that the Michaelis constant (KM) of NSP5 was 38.3 ± 4.8 μM

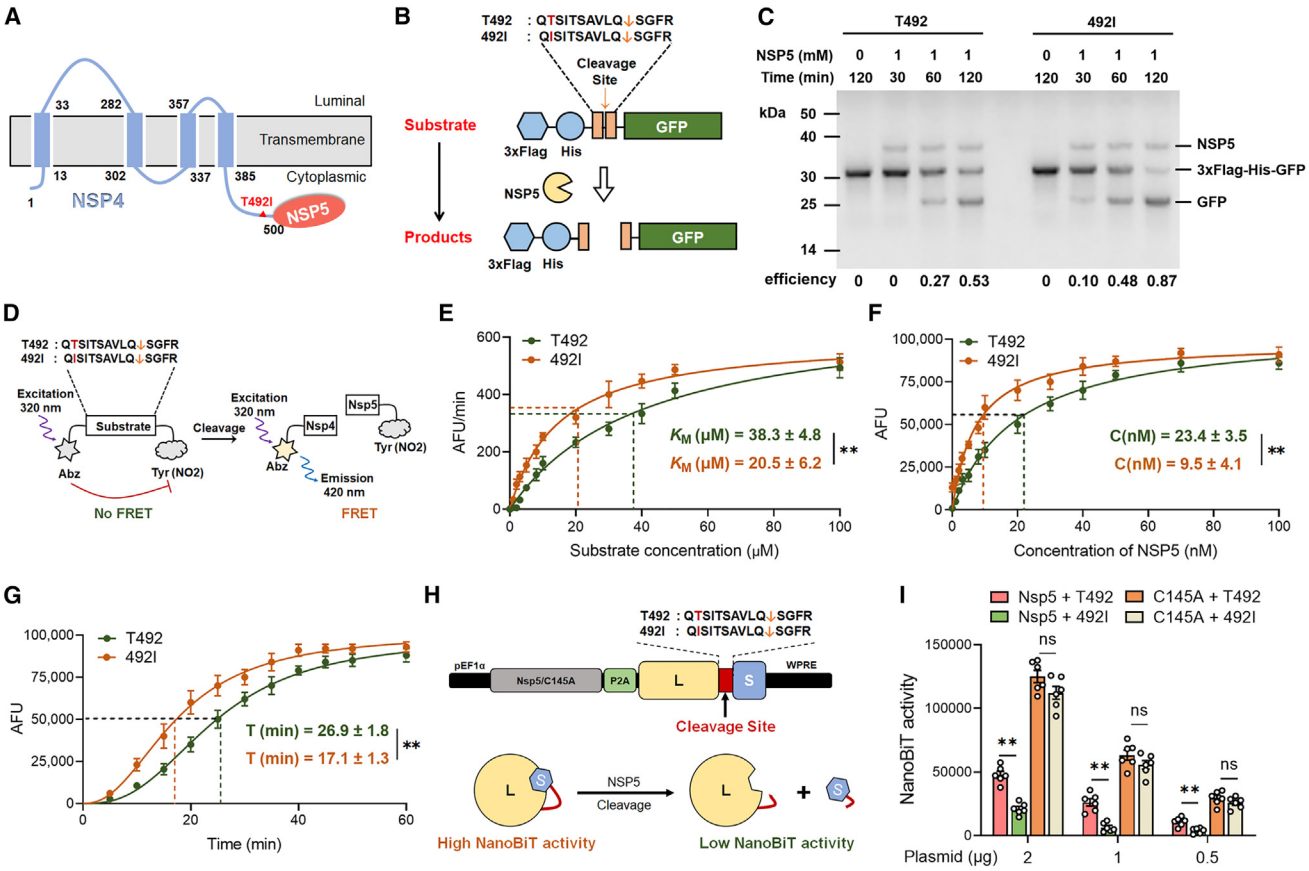

Figure 3. The T492I mutation increases the cleavage efficiency of NSP5

(A) Predicted structure of SARS-CoV-2 NSP4, a 500-amino acid protein with four predicted transmembrane domains. The mutation site (at residue 492) is indicated with a red triangle.

(B) Schematic diagram of the gel-based cleavage assay.

(C) Gel-based assay for substrate cleavage at 1 mM NSP5 over time is shown. The molecular weight of the uncleaved substrate is approximately 31-kDa, and NSP5 is approximately 35 kDa.

(D) Schematic diagram of the FRET-based protease assay. The fluorescence of Abz in the uncleaved substrate is quenched by N-tyrosine. If NSP5 cleaves the substrate, the fluorescent signal increases accordingly.

(E–G) Comparison of the enzyme kinetics of NSP5 protease on T492 and 492I substrate. KM values were determined by measuring the initial reaction rates over a range of concentrations and then plotting against the substrate concentration (E). The value of fluorescence over the increase of NSP5 concentrations is shown (F). Fluorescence intensities were detected at 20 min after the start of reaction. The value of fluorescence at 10-μM NSP5 concentration over time is shown (G). Data are presented as the mean ± SEM. Experiments were performed in triplicate.

(H) Schematic diagram of NanoBiT assay. NanoBiT is a luciferase complementation reporter comprising a large BiT (L) and a small BiT (S). The L and S fragments are connected by a linker containing the T492 or 492I cleavage site. Cleavage of the linker results in a low luciferase activity.

(I) HEK-293T cells were transfected with plasmid expressing NSP5/C145A and NanoBiT reporter as indicated, and cell lysates were collected for luciferase assay at 36 h post transfection. Experiments were performed in triplicate. Data are presented as the mean ± SEM. **p < 0.01. Abbreviation: ns, nonsignificant.

for control substrate, and 20.5 ± 6.2 μM for 492I substrate (Figure 3E). NSP5 cleavage of 492I substrate was more efficient than cleavage of control substrate (2.37-fold increase in kcat/KM; Table S5). The enzyme activity data of increase in fluorescence over increasing NSP5 concentrations (Figure 3F), as well as the data of increase in fluorescence over time at 10 μM NSP5 concentration (Figure 3G), indicated that the T492I mutation increased the cleavage efficiency of NSP5 on the NSP4|5 cleavage site.

Further, we optimized a NanoBiT assay to validate our findings. NanoBiT is comprised a Large BiT (L) and a Small BiT (S), which can complement each other to form a functional luciferase protein. We connected L and S fragments with a linker containing the NSP4|5 cleavage site. NSP5 cleaves the linker and causes L and S fragments to dissociate, resulting in a low luciferase activity (Figure 3H). The result showed that the NanoBiT activity collected from NSP5 cleavage of 492I linker group was significantly lower than that of control linker group (Figure 3I). Moreover, the catalytically inactive form of NSP5 (C145A, Cys145 was converted to Ala), which was unable to process the NSP4|5 cleavage site, was introduced to the system. We found that NSP5-C145A mutant showed no significant difference in the cleavage of control and 492I linkers (Figure 3I). These data confirm that the T492I mutation of substrate facilitates NSP5 cleavage efficiency, and the enzymatic activity remains dependent on the C145 catalytic site.

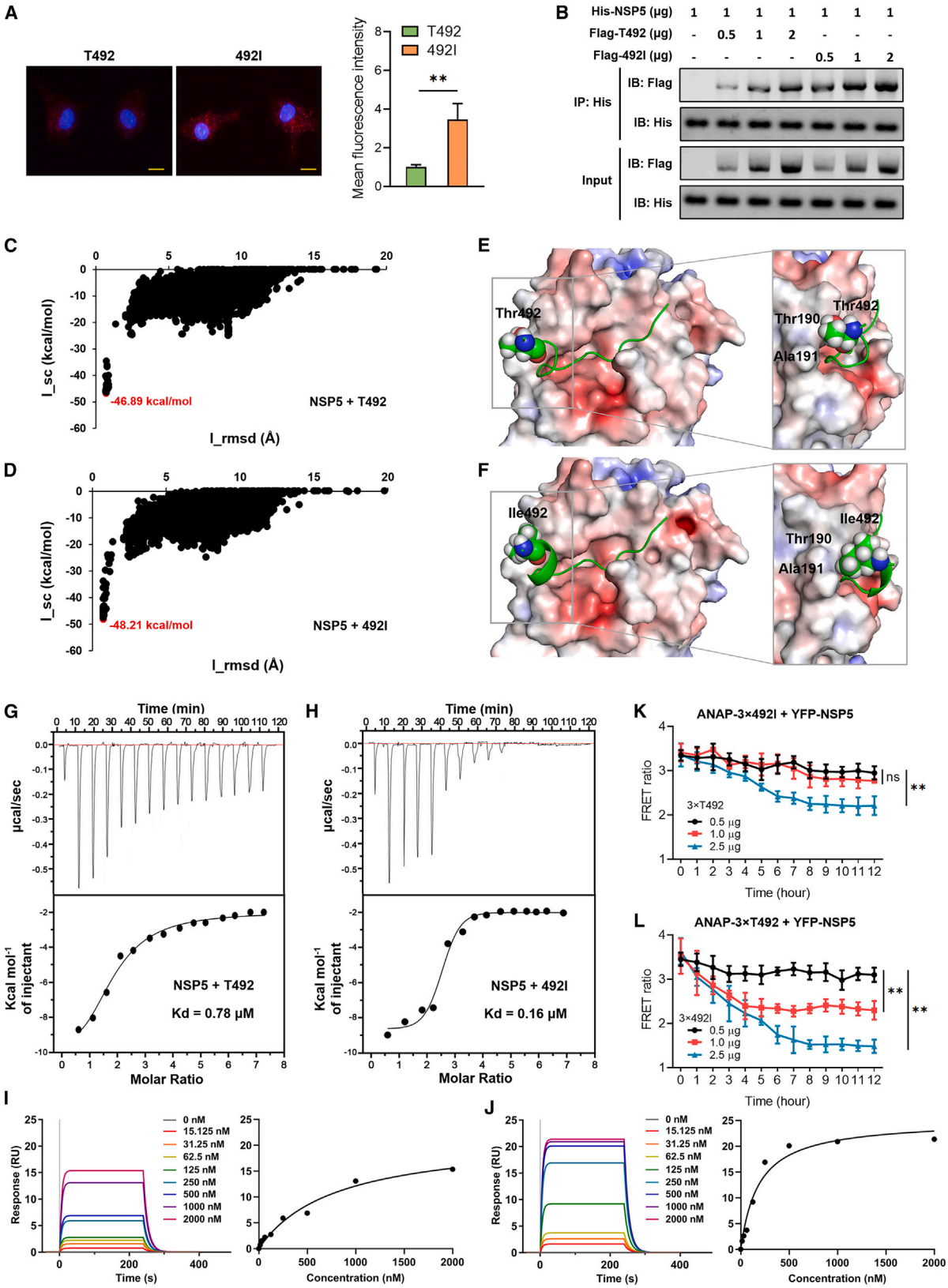

(legend on next page)

The T492I mutation enhances the NSP5-substrate contact

Next, we asked whether T492I mutation affected enzyme-substrate contact. Using a proximity ligation assay, we showed that 492I substrate can approach to the NSP5 enzyme more effectively than T492 substrate (Figure 4A). Results collected from *in vitro* co-immunoprecipitation assays showed that NSP5 enzyme bound to FLAG-tagged T492 and 492I substrates in a dose-dependent manner. In line with previous results, the binding affinity of NSP5 to the 492I substrate was stronger than that to the control substrate (Figure 4B).

To understand the structural basis of different cleavage efficiencies, we determined the 3D structures of NSP5 binding to T492 and 492I substrates. The presence of docking funnel in Figures 4C and 4D indicated that control and 492I substrates were successfully docked with SARS-CoV-2 NSP5. For each complex, the structure with the lowest interface score (I_sc) and interface root-mean-square deviation (I_rmsd) $\leq$ 4 Å from the docking trajectory was selected as a near-native model of the substrate binding to NSP5. The lowest I-sc for the T492 and 492I substrates bound complexes were −46.89 kcal/mol (Figure 4C) and −48.21 kcal/mol (Figure 4D), respectively. Compared with the control substrate, 492I mutant exhibited a relatively better binding affinity to NSP5, which is consistent with the trend of our *in vitro* and *in cellulo* experiments on protease binding activity. Furthermore, the molecular mechanism underlying the stronger binding affinity of 492I was clarified by comparing the binding patterns between the control and 492I substrates to NSP5. It was clearly shown that when the amino acid Thr at substrate 492 mutated to Ile, the latter was more suitable to form hydrophobic contacts with residues Thr190 and Ala191 in the NSP5 substrate binding pocket (Figures 4E and 4F).

Furthermore, we performed isothermal titration calorimetry (ITC) and surface plasmon resonance (SPR) to determine the accurate dissociation rate constants (K_D) of NSP5/T492 and NSP5/492I complexes. The results obtained from ITC (Figures 4G and 4H) and SPR (Figures 4I and 4J) showed that the affinity of 492I substrate to NSP5 was about 4.13–5.78 times that of T492 substrate to NSP5. Additionally, we used FRET to demonstrate that 492I substrate had a competitive advantage for NSP5 in human embryonic kidney (HEK) 293 cells. 3-(6-acetylnaphthalen-2-ylamino)-2-aminopropanoic acid (ANAP)-modified 3×492I substrate and yellow fluorescent protein (YFP)-tagged NSP5 were constructed for the intracellular FRET system (Figures S3A and S3B). FRET ratio showed that the binding of 492I substrate to NSP5 was only slightly weakened in competition with high dose of T492 substrate (Figure 4K). On the contrary, a small amount of 492I substrate was able to hijack NSP5 from the NSP5-T492 substrate complex (Figure 4L). These data collectively reveal that the T492I mutation enhances the enzyme-substrate contact, thereby increasing the protease activity of NSP5.

The T492I mutation alters SARS-CoV-2 properties by affecting NSPs

NSP5 is the main protease of SARS-CoV-2 genome and plays a major role in the cleavage of viral polyproteins. NSP5 cleaves polyproteins to generate individual functional proteins, such as RNA-dependent RNA polymerase (NSP12), helicase (NSP13), endoribonuclease (NSP15), and other indispensable cofactors. We then detected the amount of NSPs cleaved by NSP5 in Calu-3 cells infected with control and 492I virus, respectively. As a result, the protein levels of NSPs in the 492I group were consistently higher compared with the control group from 12 to 48 hpi (Figures 5A–5H), except for NSP4 (Figure 5A) and NSP8 (Figure 5D). These data validated that the T492I mutation increased the cleavage efficiency of NSP5. The protein level of structural proteins, such as nucleocapsid and spike, was also evaluated. The result showed that protein levels of N and S were not significantly altered by the T492I mutation (Figures S3C and S3D). Among the NSPs affected by T492I mutation, NSP4 and NSP6 have been reported to form a RTC along with a few host factors.[32] RTC is associated with modified host ER membranes that generate convoluted membranes (CMs) and DMVs for viral genome replication and transcription. To further confirm the impact of T492I mutation on viral life cycle, membrane rearrangement caused by viral infection was investigated by transmission electron microscopy. Analysis of virus-infected Calu-3 cells showed that T492I variant induced more extensive CMs and DMVs than control group (Figure 5I). These

Figure 4. The T492I mutation enhances the NSP5-substrate contact

(A) Proximity ligation assay of NSP5 and T492I substrates. Vero E6 cells were transfected with plasmids encoding FLAG-tagged T492 or 492I substrates. 12 h later, cells were infected with SARS-CoV-2 virus at a multiplicity of infection (MOI) of 0.01 for another 12 h. Cells were fixed, and the fluorescence intensities were detected using anti-FLAG and anti-NSP5 antibodies. The histogram on the right panel represents the mean value of fluorescence intensities. Scale bars, 10 μm.

(B) Co-immunoprecipitation assay of NSP5 and FLAG-tagged T492I substrates. His-NSP5 together with FLAG-T492I or FLAG-492I plasmids were co-transfected to HEK-293T cells as indicated. After 24 h, cell lysates were harvested and immunoprecipitated using an anti-FLAG antibody. The lower panel represents the immunoblot analysis of whole-cell lysates.

(C and D) Computational modeling for the binding of T492 and 492I substrates to SARS-CoV-2 NSP5. The Rosetta docking funnels of the T492 (C) and 492I (D) substrate to NSP5. The red plots have the lowest docking interface score (I_sc) with the interface root-mean-square deviation (I_rmsd) $\leq$ 4 Å.

(E and F) Predicted binding modes of T492 (E) and 492I (F) substrates to NSP5 corresponding to the lowest docking score in (C) and (D). The cartoon (green) and surface (APBS-generated electrostatic) models were used for the substrate and NSP5, respectively. The residues Thr492 and Ile492 were shown in sphere model.

(G and H) ITC-binding curve between the T492 (G) and 492I (H) substrate with NSP5.

(I and J) Left panels are the representative SPR sensorgrams of the response over time when increasing concentrations of T492 (I) or 492I (J) substrates were injected over purified NSP5 protein immobilized on biosensor chip. Right panels are the kinetic analysis of T492 substrate-NSP5 (I) and 492I substrate-NSP5 (J) complexes. The K_D values were determined by the steady-state affinity of each concentration.

(K and L) HEK-293T cells were transfected with CMV-3×492I(TAG)-NSP5-YFP (K) or CMV-3×T492(TAG)-NSP5-YFP (L) plasmid and then treated with 50-μM ANAP. After 18 h, cells were transfected with different dose (0.5, 1.0, and 2.5 μg, respectively) of 3×T492 (K) or 3×492I (L) plasmid. Graph displaying the FRET ratios (YFP/ANAP) recorded from single cell images. Schematic diagram of this intracellular FRET assay is shown in Figure S3. Experiments were performed in triplicate. Data are presented as the mean ± SEM. **$p < 0.01$. Abbreviation: ns, nonsignificant.

See also Figure S3.

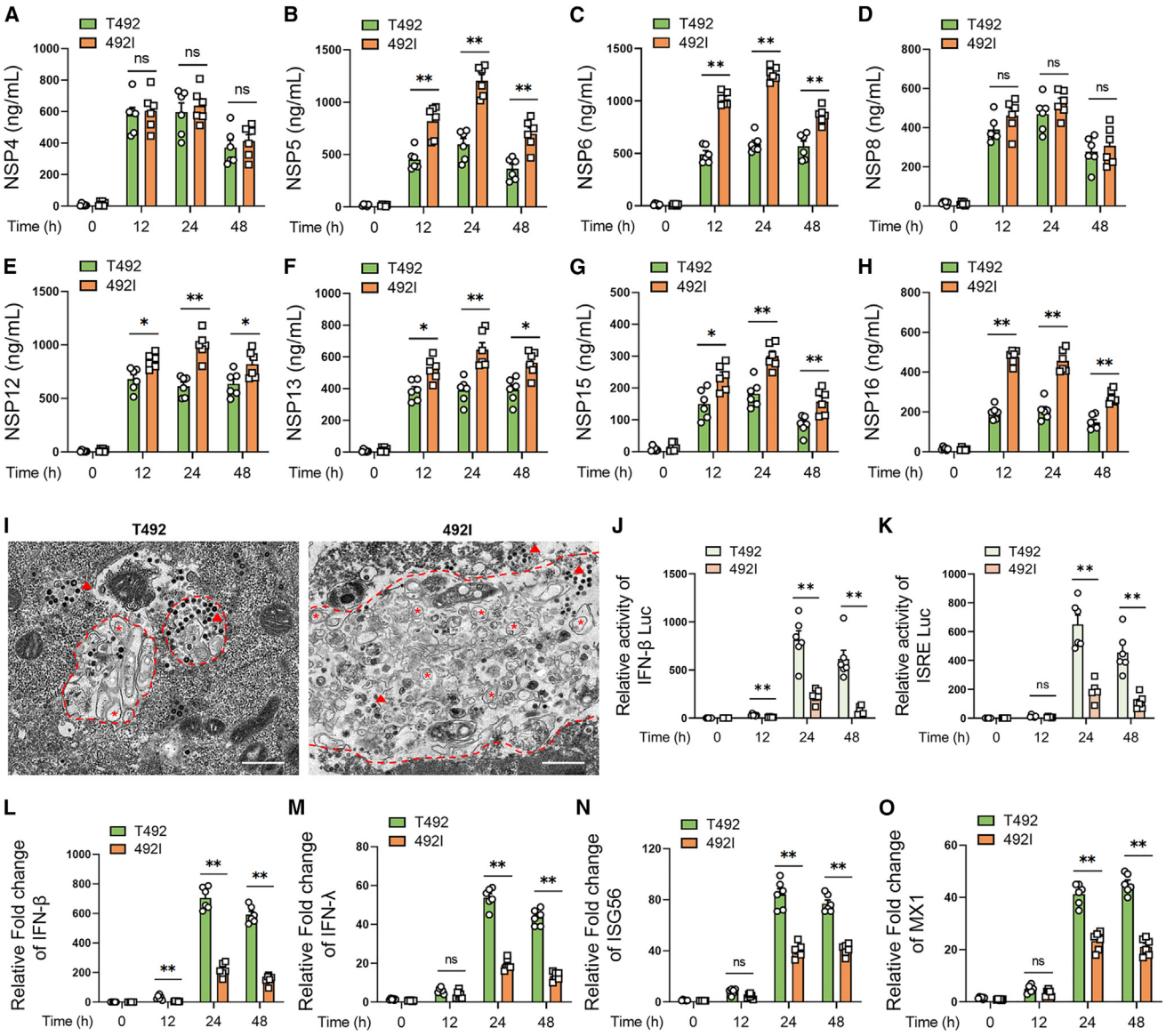

Figure 5. The T492I mutation shows an association with strengthened ability to evade host antiviral responses

(A–H) Calu-3 cells were infected with T492 or 492I virus at a MOI of 0.01. At 12, 24, and 48 h after infection, the cell lysates were harvested and subjected to ELISA analysis using specific NSP antibodies.

(I) Calu-3 cells were infected with T492 or 492I virus at a MOI of 0.01. After 48 h, cells were fixed and processed to transmission electron microscopy. Convoluted membranes are marked with red dotted lines, double-membrane vesicles are marked with red asterisks, and virus particles are marked with red arrowheads. Scale bars, 500 nm.

(J and K) Calu-3 cells were transfected with an IFN-β or ISRE luciferase reporter plasmid, along with an internal control plasmid pRL-SV40. 12 h later, cells were infected with T492 or 492I virus at a MOI of 0.01. At 12, 24, and 48 h after infection, the cell lysates were harvested and subjected to dual luciferase reporter assay.

(L–O) Calu-3 cells were infected with T492 or 492I virus at a MOI of 0.01. At 12, 24, and 48 h after infection, total RNA extracted from the cells was evaluated by qRT-PCR using a SYBR green method. The data are shown as fold change of the IFN-β (L), IFN-λ (M), ISG56 (N), and MX1 (O) mRNA levels relative to the GAPDH control. Primers are listed in Table S6A. Data in (A)–(H) and (J)–(O) are represented as the mean ± SEM. *$p < 0.05$, **$p < 0.01$. Abbreviation: ns, nonsignificant. See also Figure S3.

data are consistent with our previous result that the T492I mutation enhanced the viral replication of SARS-CoV-2 (Figures 2E and 2H).

Our *in silico* analysis predicted an association between T492I and the immune evasion capacity of SARS-CoV-2. Moreover, previous efforts reported that NSP13, NSP15, and NSP16 both serve to evade the innate immune responses of host by function as potent interferon antagonists.[44–47] We subsequently assessed the effect of T492I mutation on the IFNs and interferon-stimulated genes (ISGs) production. In comparison with the control virus, the 492I variant induced a 2.54- to 7.97-fold reduction in IFN-β and interferon-stimulated response element (ISRE)

reporters (Figures 5J and 5K). Furthermore, the T492I mutation showed a comparable inhibitory effect (2.12- to 5.68-fold) on mRNA levels of IFNs (IFN-β and IFN-λ) and representative ISGs (ISG56 and MX1) (Figures 5L–5O). These data imply that the T492I mutation of NSP4 endows SARS-CoV-2 with the ability to better evade host antiviral responses.

The T492I mutation shows an association with decreased disease severity

To understand the impact of T492I mutation on viral pathogenicity, we compared the lung lesions of hamsters infected with T492 or 492I virus. The result showed that hamsters infected with 492I virus exhibited less lung damage and pulmonary vascular congestion than the control group (Figure 6A). Interestingly, this reduction in pathogenicity was only shown at late stage of 5 dpi (Figures 6A and 6B). To validate this finding, we performed pulmonary function tests. We found that hamsters infected with 492I virus showed better residual functional capacity (Figure 6C), total lung capacity (Figure 6D), vital capacity (Figure 6E), and residual volume (Figure 6F) at 5 dpi compared with hamsters infected with T492 virus. Importantly, hamsters infected T492 virus showed a lower forced expiratory volume in 100 ms ($FEV_{0.1}$; Figure 6G) and possessed means of forced expiratory volume in 100 ms/forced vital capacity less than 0.49 ($FEV_{0.1}$/FVC, equivalent to the FEV1/FVC index in human, a criterion routinely used for pulmonary function diagnosis, less than 0.49 means severe. Figure 6H). Collectively, these data suggest that 492I virus presents decreased lung pathologies and milder pulmonary function injury in hamsters compared with the control virus.

To obtain the dynamics of pulmonary response during infection, total leukocytes recruitment (Figure 6I) and specific cell clusters (Figure 6J) were counted by flow cytometry as previously described.[48] Cell-type clusters detected in lung lobes corresponding to the leukocyte subsets included alveolar, interstitial, and monocytic macrophages, neutrophils, dendritic cells (DCs), T and natural killer (NK) cells, and B cells. The results showed that in T492 virus-infected hamsters, the peak of lung inflammation (Figure 6A) coincided with the influx of total leukocytes recruitment at 5 dpi (Figure 6I), and the cell counts of alveolar and monocytic macrophages in the T492 group were significantly higher than those in the 492I group (Figure 6J). These data indicate that the recruitment of inflammatory macrophages plays a critical role in lung damage during infection. Further, we tested the expression levels of monocytic macrophage-specific genes associated with viral RNA according to our previous report.[48] This gene set contains a range of chemokines, such as the Cysteine-Cysteine (CC) subfamily and the Cysteine-X-Cysteine (CXC) subfamily members. The results showed that 492I virus induced significantly lower levels of viral-RNA-associated chemokines in monocytic macrophages at 3 dpi when compared with control (Figure 6K). This reveals that a set of chemokines bursting at the early infection stage (3 dpi) is associated with the recruitment of inflammatory macrophages at later disease stage (5 dpi). In this context, the attenuated viral pathogenicity of the T492I mutation could be partly explained by the suppression of viral-RNA-associated chemokines in monocytic macrophages.

DISCUSSION

Our study demonstrates the transmission advantage and adaptiveness of the NSP4 T492I substitution by comprehensive *in silico* analyses and experiments. The T492I mutation arose independently within multiple lineages (Figures 1A and 1B), suggesting a universal transmission advantage of this mutation among SARS-CoV-2 lineages. The high transmissibility and dominant role in Delta sub-variants suggest a critical contribution of the T492I mutation to the fitness of Delta, Omicron, and other VOCs. The T492I mutation significantly promoted viral replication in hamster upper respiratory tracts rather than lung tissues (Figures 2H–2J), which resembles the phenotype of other adaptive mutations (S D614G, N R203K/G204R).[13,38] These data support the evolutionary trend of SARS-CoV-2 tropism toward the upper airway epithelium and away from lung tissue.[49] An increased tropism toward the upper respiratory tract may lead to increased viral productivity in tissues where angiotensin-converting enzyme 2 (ACE2) is abundantly expressed and could, at the same time, limit virus replication in the lung, where ACE2 expression is scarce. In addition, it also means faster entry into permissive cells and easier viral shedding, which in turn implies shorter incubation periods and higher rates of transmission.[49]

Mechanistically, the T492I mutation is located at the interaction region between NSP4 and NSP5. We demonstrate that the T492I mutation increases the protease activity of NSP5 by enhancing the enzyme-substrate contact. The increased protease activity eventually leads to the release of more NSPs that cleaved by NSP5. For example, NSP6 contains ER-zippering activity and acts as an organizer of DMV clusters,[31] NSP12 is a RNA-dependent RNA polymerase with nucleotidyltransferase activity, and NSP13 is a helicase with RNA 5′triphosphatase activity.[20] The elevated expression of these NSPs is partially responsible for the increased amount of CMs and may contribute to a strengthened replication and infectivity associated with the T492I mutation.

In our experimental data, NSP15 and NSP16, two NSPs cleaved by NSP5 that assist the viral immune evasion, had significantly higher protein levels in 492I group than in T492 group. Accordingly, SARS-CoV-2 variant bearing the T492I mutation showed a reinforced ability to evade host immune responses. Recently, NSP6 ΔSGF mutation has been reported to be associated with immune evasion capability.[31] Considering that all Omicron sub-variants bear both NSP4 T492I and NSP6 ΔSGF mutations, we hypothesize that the co-occurrence of these mutations may contribute to a rapid increase in infectivity and elevated immune resistance in Omicron variants.[50,51] In addition, we found that the 492I mutation reduced IFN and ISG production (Figures 5J–5O). This seems to be an alternative mechanism by which the 492I mutation allows NSP4 to recruit more membranes to the RTC, thereby improving the ability of SARS-CoV-2 to protect its RNA from double-stranded RNA (dsRNA) sensors in the cytoplasm. However, further experimental verification of these hypotheses is required.

Importantly, we found that hamsters infected with 492I virus exhibited less lung damage than those infected with T492 virus (Figures 6A and 6B), and the available clinical data support the conclusion gleaned from animal experiments (Figures 1O–1R). As a fixed mutation, T492I enhanced infectivity and immune evasion but reduced the virulence of SARS-CoV-2, suggesting

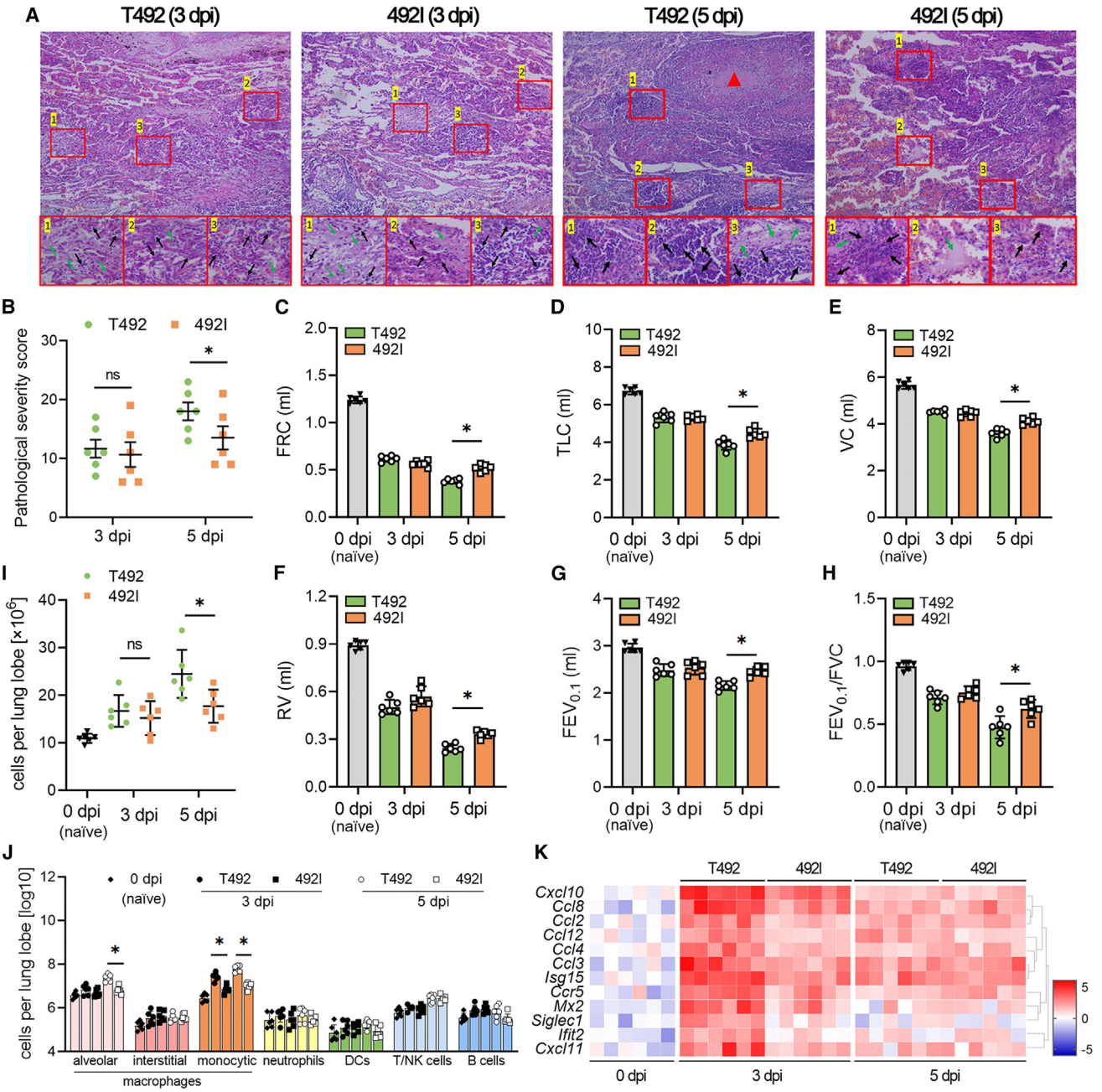

Figure 6. The T492l mutation shows an association with decreased disease severity

(A) Haemotoxylin and eosin staining of lung sections collected at 3 and 5 dpi from hamsters infected with 2 × 10^4 PFU of T492 or 492l virus. The lower photographs are magnified images of the regions denoted by rectangles in the upper photographs. The lower panel shows bronchioles with aggregation of inflammatory cells (black arrow) and surrounding alveolar wall infiltration (green arrow). Red arrowheads indicate the alveolar parenchymal lesions.

(B) Histopathology scoring of lung sections. Lung lobes were scored individually using the scoring system described in the STAR Methods. The scores of 5 slices from each hamster were added to determine the total pathology score per animal.

(C–H) Pulmonary function tests of hamsters infected with T492 or 492l virus. Functional residual capacity (C), total lung capacity (D), vital capacity (E), residual volume (F), forced expiratory volume in 100 ms (G), and forced expiratory volume in 100 ms/forced vital capacity (H) were detected at 3 and 5 dpi.

(I and J) Total leukocytes count (I) and specific cell clusters count (J) per lung lobe in hamsters infected with T492 or 492l virus and control group (naive, 0 dpi).

(K) Relative expression of monocytic macrophage-specific chemokines associated with viral RNA was detected by qRT-PCR. Coloration and point size indicate $\log_2$ fold change. Data in (B)–(J) are presented as the mean ± SEM. *$p < 0.05$. Abbreviation: ns, nonsignificant.

adaptation to changing host environments at the cost of virulence. Similarly, mutation of S78R-K79R-S81R in Japanese encephalitis virus increased the cleavage of prM protein, promoting viral replication but attenuating virulence.[52] The tropism toward airway epithelial cells, as well as the suppression of viral-RNA-associated chemokines in monocytic macrophages

by T492I may partially explain the reduced virulence of the virus. Based on this, NSP4 may be, in addition to Spike and NSP6,[27] another important protein responsible for the attenuation observed in Omicron variants. In this context, the NSP4 T492I mutation may work in concert with other spike and non-spike mutations to drive Omicron attenuation. Nevertheless, the specific mechanism underlying the attenuation of viral pathogenicity requires further in-depth investigation.

Limitations of the study

In the statistics at different geographical levels, a few countries/regions showed a decreased IF of T492I in the epidemiological survey, possibly due to the inadequacy of the sample size. Also, the mechanism by which the proteolytic activity of NSP5 contributes to the increased abundance of some but not all NSPs is unclear. In addition, the specific mechanism of the T492I mutation in evading host antiviral response should be further elucidated.

STAR★METHODS

Detailed methods are provided in the online version of this paper and include the following:

- KEY RESOURCES TABLE
- RESOURCE AVAILABILITY
  - Lead contact
  - Materials availability
  - Data and code availability
- EXPERIMENTAL MODEL AND SUBJECT DETAILS
  - SARS-CoV-2 virus
  - Cell lines
  - Hamster husbandry and infection
  - Human airway tissue culture infection
- METHOD DETAILS
  - Statistics of SARS-CoV-2 mutations and VOCs
  - The inference of relative fitness based on global vaccination coverage data
  - Function prediction based on clinical data
  - Plaque assay, viral subgenomic RNA assay and genomic RNA assay
  - Competition assay
  - Pathological examination and scoring
  - Pulmonary function test
  - Protein structure modeling and docking of NSP5 and substrates
  - Immunoprecipitation and immunoblot assay
  - Dual luciferase reporter assay
  - Real-time qRT-PCR
  - Enzyme linked immunosorbent assay
  - Proximity ligation assay
  - Isothermal titration calorimetry and Surface plasmon resonance
  - Intracellular fluorescence resonance energy transfer
  - Statistical Analysis

SUPPLEMENTAL INFORMATION

Supplemental information can be found online at https://doi.org/10.1016/j.chom.2023.06.002.

ACKNOWLEDGMENTS

We gratefully acknowledge the submitting and the originating laboratories where genetic sequence data were generated and shared via NCBI and the GISAID Initiative. This work was supported by grants from the National Natural Science Foundation of China, SGC's Rapid Response Funding for COVID-19 (C-0002), the National Natural Science Foundation of China (81970008, 32170661, and 82000020), the Fundamental Research Funds for the Central Universities (2019CDYGZD-009 and 2021CDJYGRH-009), Chongqing Talents: Exceptional Young Talents Project (cstc2021ycjhbgzxm0099), and the Youth Innovative Talents Training Project of Chongqing (CY210102). The funders had no role in study design, data collection and analysis, decision to publish, or preparation of the manuscript.

AUTHOR CONTRIBUTIONS

H.W., Z.Z., X.L., and C.J. collected the data and performed the population genetic analyses. H.W., X.L., Z.S., W.X., J.T., D.K., and Y.X. performed the experiments. W.X. and B.X. performed the protein structure analysis. H.W. conceived the idea. H.W., Z.Z., X.L., and Z.S. wrote the manuscript. H.W., W.X., and Z.Z. coordinated the project.

DECLARATION OF INTERESTS

The authors declare no competing interests.

Received: January 29, 2023
Revised: April 13, 2023
Accepted: June 9, 2023
Published: July 3, 2023

REFERENCES

1. Ralph, R., Lew, J., Zeng, T., Francis, M., Xue, B., Roux, M., Toloue Ostadgavahi, A., Rubino, S., Dawe, N.J., Al-Ahdal, M.N., et al. (2020). 2019-nCoV (Wuhan virus), a novel coronavirus: human-to-human transmission, travel-related cases, and vaccine readiness. J. Infect. Dev. Ctries. *14*, 3–17. https://doi.org/10.3855/jidc.12425.
2. Hui, D.S., I Azhar, E., Madani, T.A., Ntoumi, F., Kock, R., Dar, O., Ippolito, G., Mchugh, T.D., Memish, Z.A., Drosten, C., et al. (2020). The continuing 2019-nCoV epidemic threat of novel coronaviruses to global health - the latest 2019 novel coronavirus outbreak in Wuhan, China. Int. J. Infect. Dis. *91*, 264–266. https://doi.org/10.1016/j.ijid.2020.01.009.
3. Smith, E.C., Blanc, H., Surdel, M.C., Vignuzzi, M., and Denison, M.R. (2013). Coronaviruses lacking exoribonuclease activity are susceptible to lethal mutagenesis: evidence for proofreading and potential therapeutics. PLoS Pathog. *9*, e1003565. https://doi.org/10.1371/journal.ppat.1003565.
4. Wu, F., Zhao, S., Yu, B., Chen, Y.M., Wang, W., Song, Z.G., Hu, Y., Tao, Z.W., Tian, J.H., Pei, Y.Y., et al. (2020). A new coronavirus associated with human respiratory disease in China. Nature *579*, 265–269. https://doi.org/10.1038/s41586-020-2008-3.
5. Mercatelli, D., and Giorgi, F.M. (2020). Geographic and genomic distribution of SARS-CoV-2 mutations. Front. Microbiol. *11*, 1800. https://doi.org/10.3389/fmicb.2020.01800.
6. Korber, B., Fischer, W.M., Gnanakaran, S., Yoon, H., Theiler, J., Abfalterer, W., Hengartner, N., Giorgi, E.E., Bhattacharya, T., Foley, B., et al. (2020). Tracking changes in SARS-CoV-2 spike: evidence that D614G increases infectivity of the COVID-19 virus. Cell *182*, 812–827.e19. https://doi.org/10.1016/j.cell.2020.06.043.
7. Trucchi, E., Gratton, P., Mafessoni, F., Motta, S., Cicconardi, F., Mancia, F., Bertorelle, G., D'Annessa, I., and Di Marino, D. (2021). Population dynamics and structural effects at Short and Long Range support the hypothesis of the selective advantage of the G614 SARS-CoV-2 spike variant. Mol. Biol. Evol. *38*, 1966–1979. https://doi.org/10.1093/molbev/msaa337.

8. Zhu, Z., Liu, G., Meng, K., Yang, L., Liu, D., and Meng, G. (2021). Rapid spread of mutant alleles in worldwide SARS-CoV-2 strains revealed by genome-wide single nucleotide polymorphism and variation analysis. Genome Biol. Evol. *13*, evab015. https://doi.org/10.1093/gbe/evab015.

9. Cheng, L., Song, S., Zhou, B., Ge, X., Yu, J., Zhang, M., Ju, B., and Zhang, Z. (2021). Impact of the N501Y substitution of SARS-CoV-2 Spike on neutralizing monoclonal antibodies targeting diverse epitopes. Virol. J. *18*, 87. https://doi.org/10.1186/s12985-021-01554-8.

10. Zhao, S., Lou, J., Cao, L., Zheng, H., Chong, M.K.C., Chen, Z., Chan, R.W.Y., Zee, B.C.Y., Chan, P.K.S., and Wang, M.H. (2021). Quantifying the transmission advantage associated with N501Y substitution of SARS-CoV-2 in the United Kingdom: an early data-driven analysis. J. Travel Med. *28*, taab011. https://doi.org/10.1093/jtm/taab011.

11. Liu, Y., Liu, J., Plante, K.S., Plante, J.A., Xie, X., Zhang, X., Ku, Z., An, Z., Scharton, D., Schindewolf, C., et al. (2022). The N501Y spike substitution enhances SARS-CoV-2 infection and transmission. Nature *602*, 294–299. https://doi.org/10.1038/s41586-021-04245-0.

12. Garcia-Beltran, W.F., Lam, E.C., St Denis, K., Nitido, A.D., Garcia, Z.H., Hauser, B.M., Feldman, J., Pavlovic, M.N., Gregory, D.J., Poznansky, M.C., et al. (2021). Multiple SARS-CoV-2 variants escape neutralization by vaccine-induced humoral immunity. Cell *184*, 2372–2383.e9. https://doi.org/10.1016/j.cell.2021.03.013.

13. Wu, H., Xing, N., Meng, K., Fu, B., Xue, W., Dong, P., Tang, W., Xiao, Y., Liu, G., Luo, H., et al. (2021). Nucleocapsid mutations R203K/G204R increase the infectivity, fitness, and virulence of SARS-CoV-2. Cell Host Microbe *29*, 1788–1801.e6. https://doi.org/10.1016/j.chom.2021.11.005.

14. Motozono, C., Toyoda, M., Zahradnik, J., Saito, A., Nasser, H., Tan, T.S., Ngare, I., Kimura, I., Uriu, K., Kosugi, Y., et al. (2021). SARS-CoV-2 spike L452R variant evades cellular immunity and increases infectivity. Cell Host Microbe *29*, 1124–1136.e11. https://doi.org/10.1016/j.chom.2021.06.006.

15. Deng, X., Garcia-Knight, M.A., Khalid, M.M., Servellita, V., Wang, C., Morris, M.K., Sotomayor-González, A., Glasner, D.R., Reyes, K.R., Gliwa, A.S., et al. (2021). Transmission, infectivity, and neutralization of a spike L452R SARS-CoV-2 variant. Cell *184*, 3426–3437.e8. https://doi.org/10.1016/j.cell.2021.04.025.

16. Jung, C., Kmiec, D., Koepke, L., Zech, F., Jacob, T., Sparrer, K.M.J., and Kirchhoff, F. (2022). Omicron: what makes the latest SARS-CoV-2 variant of concern so concerning? J. Virol. *96*, e0207721. https://doi.org/10.1128/jvi.02077-21.

17. Pastorio, C., Zech, F., Noettger, S., Jung, C., Jacob, T., Sanderson, T., Sparrer, K.M.J., and Kirchhoff, F. (2022). Determinants of Spike infectivity, processing, and neutralization in SARS-CoV-2 Omicron subvariants BA.1 and BA.2. Cell Host Microbe *30*, 1255–1268.e5. https://doi.org/10.1016/j.chom.2022.07.006.

18. Hussain, M., Jabeen, N., Raza, F., Shabbir, S., Baig, A.A., Amanullah, A., and Aziz, B. (2020). Structural variations in human ACE2 may influence its binding with SARS-CoV-2 spike protein. J. Med. Virol. *92*, 1580–1586. https://doi.org/10.1002/jmv.25832.

19. Salvatori, G., Luberto, L., Maffei, M., Aurisicchio, L., Roscilli, G., Palombo, F., and Marra, E. (2020). SARS-CoV-2 SPIKE PROTEIN: an optimal immunological target for vaccines. J. Transl. Med. *18*, 222. https://doi.org/10.1186/s12967-020-02392-y.

20. V'Kovski, P., Kratzel, A., Steiner, S., Stalder, H., and Thiel, V. (2021). Coronavirus biology and replication: implications for SARS-CoV-2. Nat. Rev. Microbiol. *19*, 155–170. https://doi.org/10.1038/s41579-020-00468-6.

21. Sims, A.C., Ostermann, J., and Denison, M.R. (2000). Mouse hepatitis virus replicase proteins associate with two distinct populations of intracellular membranes. J. Virol. *74*, 5647–5654. https://doi.org/10.1128/jvi.74.12.5647-5654.2000.

22. Brockway, S.M., Lu, X.T., Peters, T.R., Dermody, T.S., and Denison, M.R. (2004). Intracellular localization and protein interactions of the gene 1 protein p28 during mouse hepatitis virus replication. J. Virol. *78*, 11551–11562. https://doi.org/10.1128/JVI.78.21.11551-11562.2004.

23. Gosert, R., Kanjanahaluethai, A., Egger, D., Bienz, K., and Baker, S.C. (2002). RNA replication of mouse hepatitis virus takes place at double-membrane vesicles. J. Virol. *76*, 3697–3708. https://doi.org/10.1128/jvi.76.8.3697-3708.2002.

24. Zhang, K., Miorin, L., Makio, T., Dehghan, I., Gao, S., Xie, Y., Zhong, H., Esparza, M., Kehrer, T., Kumar, A., et al. (2021). Nsp1 protein of SARS-CoV-2 disrupts the mRNA export machinery to inhibit host gene expression. Sci. Adv. *7*, eabe7386. https://doi.org/10.1126/sciadv.abe7386.

25. Fehr, A.R., Athmer, J., Channappanavar, R., Phillips, J.M., Meyerholz, D.K., and Perlman, S. (2015). The nsp3 macrodomain promotes virulence in mice with coronavirus-induced encephalitis. J. Virol. *89*, 1523–1536. https://doi.org/10.1128/JVI.02596-14.

26. Kumar, A., Prasoon, P., Kumari, C., Pareek, V., Faiq, M.A., Narayan, R.K., Kulandhasamy, M., and Kant, K. (2021). SARS-CoV-2-specific virulence factors in COVID-19. J. Med. Virol. *93*, 1343–1350. https://doi.org/10.1002/jmv.26615.

27. Chen, D.Y., Chin, C.V., Kenney, D., Tavares, A.H., Khan, N., Conway, H.L., Liu, G., Choudhary, M.C., Gertje, H.P., O'Connell, A.K., et al. (2023). Spike and nsp6 are key determinants of SARS-CoV-2 Omicron BA.1 attenuation. Nature *615*, 143–150. https://doi.org/10.1038/s41586-023-05697-2.

28. Halfmann, P.J., Iida, S., Iwatsuki-Horimoto, K., Maemura, T., Kiso, M., Scheaffer, S.M., Darling, T.L., Joshi, A., Loeber, S., Singh, G., et al. (2022). SARS-CoV-2 Omicron virus causes attenuated disease in mice and hamsters. Nature *603*, 687–692. https://doi.org/10.1038/s41586-022-04441-6.

29. Chen, D.Y., Kenney, D., Chin, C.V., Tavares, A.H., Khan, N., Conway, H.L., Liu, G., Choudhary, M.C., Gertje, H.P., O'Connell, A.K., et al. (2023). Role of spike in the pathogenic and antigenic behavior of SARS-CoV-2 BA.1 Omicron. https://doi.org/10.1101/2022.10.13.512134.

30. Wolff, G., Melia, C.E., Snijder, E.J., and Bárcena, M. (2020). Double-membrane vesicles as platforms for viral replication. Trends Microbiol. *28*, 1022–1033. https://doi.org/10.1016/j.tim.2020.05.009.

31. Ricciardi, S., Guarino, A.M., Giaquinto, L., Polishchuk, E.V., Santoro, M., Di Tullio, G., Wilson, C., Panariello, F., Soares, V.C., Dias, S.S.G., et al. (2022). The role of NSP6 in the biogenesis of the SARS-CoV-2 replication organelle. Nature *606*, 761–768. https://doi.org/10.1038/s41586-022-04835-6.

32. Angelini, M.M., Akhlaghpour, M., Neuman, B.W., and Buchmeier, M.J. (2013). Severe acute respiratory syndrome coronavirus nonstructural proteins 3, 4, and 6 induce double-membrane vesicles. mBio *4*. e00524–e00513. https://doi.org/10.1128/mBio.00524-13.

33. Faizan, M.I., Chaudhuri, R., Sagar, S., Albogami, S., Chaudhary, N., Azmi, I., Akhtar, A., Ali, S.M., Kumar, R., Iqbal, J., et al. (2022). NSP4 and ORF9b of SARS-CoV-2 induce pro-inflammatory mitochondrial DNA release in inner membrane-derived vesicles. Cells *11*, 2969. https://doi.org/10.3390/cells11192969.

34. Yang, L., Xie, X., Tu, Z., Fu, J., Xu, D., and Zhou, Y. (2021). The signal pathways and treatment of cytokine storm in COVID-19. Signal Transduct. Target. Ther. *6*, 255. https://doi.org/10.1038/s41392-021-00679-0.

35. Del Valle, D.M., Kim-Schulze, S., Huang, H.H., Beckmann, N.D., Nirenberg, S., Wang, B., Lavin, Y., Swartz, T.H., Madduri, D., Stock, A., et al. (2020). An inflammatory cytokine signature predicts COVID-19 severity and survival. Nat. Med. *26*, 1636–1643. https://doi.org/10.1038/s41591-020-1051-9.

36. Hadfield, J., Megill, C., Bell, S.M., Huddleston, J., Potter, B., Callender, C., Sagulenko, P., Bedford, T., and Neher, R.A. (2018). Nextstrain: real-time tracking of pathogen evolution. Bioinformatics *34*, 4121–4123. https://doi.org/10.1093/bioinformatics/bty407.

37. Shu, Y., and McCauley, J. (2017). GISAID: global initiative on sharing all influenza data - from vision to reality. Euro Surveill. *22*, 30494. https://doi.org/10.2807/1560-7917.ES.2017.22.13.30494.

38. Plante, J.A., Liu, Y., Liu, J., Xia, H., Johnson, B.A., Lokugamage, K.G., Zhang, X., Muruato, A.E., Zou, J., Fontes-Garfias, C.R., et al. (2021). Spike mutation D614G alters SARS-CoV-2 fitness. Nature *592*, 116–121. https://doi.org/10.1038/s41586-020-2895-3.

39. Xie, X., Lokugamage, K.G., Zhang, X., Vu, M.N., Muruato, A.E., Menachery, V.D., and Shi, P.Y. (2021). Engineering SARS-CoV-2 using a reverse genetic system. Nat. Protoc. *16*, 1761–1784. https://doi.org/10.1038/s41596-021-00491-8.

40. Scott, B.M., Lacasse, V., Blom, D.G., Tonner, P.D., and Blom, N.S. (2022). Predicted coronavirus Nsp5 protease cleavage sites in the human proteome. BMC Genom. Data *23*, 25. https://doi.org/10.1186/s12863-022-01044-y.

41. Lee, J., Kenward, C., Worrall, L.J., Vuckovic, M., Gentile, F., Ton, A.T., Ng, M., Cherkasov, A., Strynadka, N.C.J., and Paetzel, M. (2022). X-ray crystallographic characterization of the SARS-CoV-2 main protease polyprotein cleavage sites essential for viral processing and maturation. Nat. Commun. *13*, 5196. https://doi.org/10.1038/s41467-022-32854-4.

42. MacDonald, E.A., Frey, G., Namchuk, M.N., Harrison, S.C., Hinshaw, S.M., and Windsor, I.W. (2021). Recognition of divergent viral substrates by the SARS-CoV-2 main protease. ACS Infect. Dis. *7*, 2591–2595. https://doi.org/10.1021/acsinfecdis.1c00237.

43. Muramatsu, T., Takemoto, C., Kim, Y.T., Wang, H., Nishii, W., Terada, T., Shirouzu, M., and Yokoyama, S. (2016). SARS-CoV 3CL protease cleaves its C-terminal autoprocessing site by novel subsite cooperativity. Proc. Natl. Acad. Sci. USA *113*, 12997–13002. https://doi.org/10.1073/pnas.1601327113.

44. Yuen, C.K., Lam, J.Y., Wong, W.M., Mak, L.F., Wang, X., Chu, H., Cai, J.P., Jin, D.Y., To, K.K., Chan, J.F., et al. (2020). SARS-CoV-2 nsp13, nsp14, nsp15 and orf6 function as potent interferon antagonists. Emerg. Microbes Infect. *9*, 1418–1428. https://doi.org/10.1080/22221751.2020.1780953.

45. Lei, X., Dong, X., Ma, R., Wang, W., Xiao, X., Tian, Z., Wang, C., Wang, Y., Li, L., Ren, L., et al. (2020). Activation and evasion of type I interferon responses by SARS-CoV-2. Nat. Commun. *11*, 3810. https://doi.org/10.1038/s41467-020-17665-9.

46. Xia, H., Cao, Z., Xie, X., Zhang, X., Chen, J.Y., Wang, H., Menachery, V.D., Rajsbaum, R., and Shi, P.Y. (2020). Evasion of Type I interferon by SARS-CoV-2. Cell Rep. *33*, 108234. https://doi.org/10.1016/j.celrep.2020.108234.

47. Schindewolf, C., Lokugamage, K., Vu, M.N., Johnson, B.A., Scharton, D., Plante, J.A., Kalveram, B., Crocquet-Valdes, P.A., Sotcheff, S., Jaworski, E., et al. (2023). SARS-CoV-2 uses nonstructural Protein 16 to evade restriction by IFIT1 and IFIT3. J. Virol. *97*, e0153222. https://doi.org/10.1128/jvi.01532-22.

48. Nouailles, G., Wyler, E., Pennitz, P., Postmus, D., Vladimirova, D., Kazmierski, J., Pott, F., Dietert, K., Muelleder, M., Farztdinov, V., et al. (2021). Temporal omics analysis in Syrian hamsters unravel cellular effector responses to moderate COVID-19. Nat. Commun. *12*, 4869. https://doi.org/10.1038/s41467-021-25030-7.

49. Liu, Y. (2023). Attenuation and degeneration of SARS-CoV-2 despite adaptive evolution. Cureus *15*, e33316. https://doi.org/10.7759/cureus.33316.

50. Zhang, L., Li, Q., Liang, Z., Li, T., Liu, S., Cui, Q., Nie, J., Wu, Q., Qu, X., Huang, W., and Wang, Y. (2022). The significant immune escape of pseudotyped SARS-CoV-2 variant Omicron. Emerg. Microbes Infect. *11*, 1–5. https://doi.org/10.1080/22221751.2021.2017757.

51. Cao, Y., Wang, J., Jian, F., Xiao, T., Song, W., Yisimayi, A., Huang, W., Li, Q., Wang, P., An, R., et al. (2022). Omicron escapes the majority of existing SARS-CoV-2 neutralizing antibodies. Nature *602*, 657–663. https://doi.org/10.1038/s41586-021-04385-3.

52. Xiong, J., Yan, M., Zhu, S., Zheng, B., Wei, N., Yang, L., Si, Y., Cao, S., and Ye, J. (2022). Increased cleavage of Japanese encephalitis virus prM protein promotes viral replication but attenuates virulence. Microbiol. Spectr. *10*, e0141722. https://doi.org/10.1128/spectrum.01417-22.

53. Stajich, J.E. (2007). An introduction to BioPerl. Methods Mol. Biol. *406*, 535–548. https://doi.org/10.1007/978-1-59745-535-0_26.

54. Edgar, R.C. (2004). MUSCLE: a multiple sequence alignment method with reduced time and space complexity. BMC Bioinformatics *5*, 113. https://doi.org/10.1186/1471-2105-5-113.

55. Li, H. (2011). A statistical framework for SNP calling, mutation discovery, association mapping and population genetical parameter estimation from sequencing data. Bioinformatics *27*, 2987–2993. https://doi.org/10.1093/bioinformatics/btr509.

56. Price, M.N., Dehal, P.S., and Arkin, A.P. (2010). FastTree 2--approximately maximum-likelihood trees for large alignments. PLoS One *5*, e9490. https://doi.org/10.1371/journal.pone.0009490.

57. Balaban, M., Moshiri, N., Mai, U., Jia, X., and Mirarab, S. (2019). TreeCluster: clustering biological sequences using phylogenetic trees. PLoS One *14*, e0221068. https://doi.org/10.1371/journal.pone.0221068.

58. Suchard, M.A., Lemey, P., Baele, G., Ayres, D.L., Drummond, A.J., and Rambaut, A. (2018). Bayesian phylogenetic and phylodynamic data integration using BEAST 1.10. Virus Evol. *4*, vey016. https://doi.org/10.1093/ve/vey016.

59. Rambaut, A., Drummond, A.J., Xie, D., Baele, G., and Suchard, M.A. (2018). Posterior summarization in Bayesian phylogenetics using Tracer 1.7. Syst. Biol. *67*, 901–904. https://doi.org/10.1093/sysbio/syy032.

60. Bouckaert, R., Vaughan, T.G., Barido-Sottani, J., Duchêne, S., Fourment, M., Gavryushkina, A., Heled, J., Jones, G., Kühnert, D., De Maio, N., et al. (2019). BEAST 2.5: an advanced software platform for Bayesian evolutionary analysis. PLoS Comput. Biol. *15*, e1006650. https://doi.org/10.1371/journal.pcbi.1006650.

61. Volz, E.M., and Siveroni, I. (2018). Bayesian phylodynamic inference with complex models. PLoS Comput. Biol. *14*, e1006546. https://doi.org/10.1371/journal.pcbi.1006546.

62. Zhu, Z., Meng, K., Liu, G., and Meng, G. (2021). A database resource and online analysis tools for coronaviruses on a historical and global scale. Database (Oxford) *2020*, baaa070. https://doi.org/10.1093/database/baaa070.

63. Xie, X., Muruato, A., Lokugamage, K.G., Narayanan, K., Zhang, X., Zou, J., Liu, J., Schindewolf, C., Bopp, N.E., Aguilar, P.V., et al. (2020). An infectious cDNA clone of SARS-CoV-2. Cell Host Microbe *27*, 841–848.e3. https://doi.org/10.1016/j.chom.2020.04.004.

64. Thi Nhu Thao, T., Labroussaa, F., Ebert, N., V'kovski, P., Stalder, H., Portmann, J., Kelly, J., Steiner, S., Holwerda, M., Kratzel, A., et al. (2020). Rapid reconstruction of SARS-CoV-2 using a synthetic genomics platform. Nature *582*, 561–565. https://doi.org/10.1038/s41586-020-2294-9.

65. Liao, X., and Meyer, M.C. (2019). cgam: an R package for the Constrained Generalized Additive Model. J. Stat. Software *89*, 1–24. https://doi.org/10.18637/jss.v089.i05.

66. Volz, E., Hill, V., McCrone, J.T., Price, A., Jorgensen, D., O'Toole, Á., Southgate, J., Johnson, R., Jackson, B., Nascimento, F.F., et al. (2021). Evaluating the effects of SARS-CoV-2 spike mutation D614G on transmissibility and pathogenicity. Cell *184*, 64–75.e11. https://doi.org/10.1016/j.cell.2020.11.020.

67. Volz, E.M., and Didelot, X. (2018). Modeling the growth and decline of pathogen effective population size provides insight into epidemic dynamics and drivers of antimicrobial resistance. Syst. Biol. *67*, 719–728. https://doi.org/10.1093/sysbio/syy007.

68. Hamilton, M.B. (2009). Population Genetics (John Wiley & Sons, Ltd.).

69. Corman, V.M., Landt, O., Kaiser, M., Molenkamp, R., Meijer, A., Chu, D.K., Bleicker, T., Brünink, S., Schneider, J., Schmidt, M.L., et al. (2020). Detection of 2019 novel coronavirus (2019-nCoV) by real-time RT-PCR. Euro Surveill. *25*, 2000045. https://doi.org/10.2807/1560-7917.ES.2020.25.3.2000045.

70. Dagotto, G., Mercado, N.B., Martinez, D.R., Hou, Y.J., Nkolola, J.P., Carnahan, R.H., Crowe, J.E., Jr., Baric, R.S., and Barouch, D.H. (2021). Comparison of subgenomic and total RNA in SARS-CoV-2 challenged rhesus macaques. J. Virol. *95*. e02370–e02320. https://doi.org/10.1128/JVI.02370-20.

71. Marchand, E., De Leyn, P., Gayan-Ramirez, G., Palecek, F., de Bock, V., Dom, R., and Decramer, M. (2000). Lung volume reduction surgery does not improve diaphragmatic contractile properties or atrophy in hamsters

with elastase-induced emphysema. Am. J. Respir. Crit. Care Med. *162*, 1052–1057. https://doi.org/10.1164/ajrccm.162.3.9911096.

72. Marchand, E., De, L.P., Gayan-Ramirez, G., Palecek, F., Verbeken, E., and Decramer, M. (2002). Effects of lung volume reduction surgery in hamsters with elastase-induced emphysema. Eur. Respir. J. *19*, 422–428. https://doi.org/10.1183/09031936.02.01532001.
73. Zhao, Y., Zhu, Y., Liu, X., Jin, Z., Duan, Y., Zhang, Q., Wu, C., Feng, L., Du, X., Zhao, J., et al. (2022). Structural basis for replicase polyprotein cleavage and substrate specificity of main protease from SARS-CoV-2. Proc. Natl. Acad. Sci. USA *119*, e2117142119. https://doi.org/10.1073/pnas.2117142119.
74. Huang, P.S., Ban, Y.E., Richter, F., Andre, I., Vernon, R., Schief, W.R., and Baker, D. (2011). RosettaRemodel: a generalized framework for flexible backbone protein design. PloS One *6*, e24109. https://doi.org/10.1371/journal.pone.0024109.
75. Alford, R.F., Leaver-Fay, A., Jeliazkov, J.R., O'Meara, M.J., DiMaio, F.P., Park, H., Shapovalov, M.V., Renfrew, P.D., Mulligan, V.K., Kappel, K., et al. (2017). The Rosetta all-atom energy function for macromolecular modeling and design. J. Chem. Theor. Comput. *13*, 3031–3048. https://doi.org/10.1021/acs.jctc.7b00125.
76. Park, S.H., Ko, W., Lee, H.S., and Shin, I. (2019). Analysis of protein-protein interaction in a single live cell by using a FRET system based on genetic code expansion technology. J. Am. Chem. Soc. *141*, 4273–4281. https://doi.org/10.1021/jacs.8b10098.

STAR★METHODS

KEY RESOURCES TABLE

REAGENT or RESOURCE	SOURCE	IDENTIFIER
Chemicals, Peptides, and Recombinant Proteins		
mMESSAGE mMACHINE T7 Transcription Kit	Thermo Fisher Scientific	Cat#AM1344
GeneJET PCR Purification kit	Thermo Fisher Scientific	Cat#K0701
RNeasy Mini Kit	QIAGEN	Cat#74104
NEB Golden Gate Assembly Kit (BsaI-HFv2)	New England Biolabs	Cat#E1601L
Lipofectamine 3000 Transfection Reagent	Thermo Fisher Scientific	Cat#L3000015
SuperScript III One-Step RT–PCR kit	Thermo Fisher Scientific	Cat#12574018
iTaq Universal SYBR Green One-Step Kit	Bio-Rad	Cat#1725150
RIPA Lysis Buffer	Merck Millipore	Cat#20-188
Protease Inhibitor Cocktail I	Merck Millipore	Cat#20-201
Dual Luciferase Reporter Assay System	Promega	Cat#E1501
Protein A-Agarose	Santa Cruz Biotechnology	Cat#sc-2001
anti-His antibody	Santa Cruz Biotechnology	Cat#sc-8036; RRID:AB_627727
anti-Flag antibody	Thermo Fisher Scientific	Cat#MA1-91878; RRID:AB_1957945
anti-NSP4 antibody	Merck Millipore	Cat#SAB3501139; RRID:AB_2938790
anti-NSP5 antibody	Merck Millipore	Cat#SAB3501127; RRID:AB_2938789
anti-NSP6 antibody	Merck Millipore	Cat#SAB3501140; RRID:AB_2938788
anti-NSP8 antibody	Merck Millipore	Cat#SAB3501131; RRID:AB_2938787
anti-NSP12 antibody	Novus Biologicals	Cat#NBP3-07963; RRID:AB_2938786
anti-NSP13 antibody	Novus Biologicals	Cat#NBP3-07055; RRID:AB_2938785
anti-NSP15 antibody	Novus Biologicals	Cat#NBP3-11932; RRID:AB_2938784
anti-NSP16 antibody	ABclonal	Cat#A20283; RRID:AB_2891177
anti-Nucleocapsid antibody	Thermo Fisher Scientific	Cat#MA5-42337; RRID:AB_2911478
anti-Spike antibody	Thermo Fisher Scientific	Cat#MA5-42338; RRID:AB_2911479
Experimental Models: Cell Lines		
Vero E6 cells	ATCC	CRL-1586
Calu-3 cells	ATCC	HTB-55
HEK-293T cells	ATCC	CRL-3216
Oligonucleotides		
SARS-CoV-2 F1-F7 sequences	Wu et al.[13]	Methods S1
Primers for real-time qRT-PCR	Integrated DNA Technologies	Table S6A
Primers for overlap-extension PCR	Integrated DNA Technologies	Table S6B
Primers for viral sgRNA assay	Wu et al.[13]	Table S6C
Primers for viral genomic RNA assay	Wu et al.[13]	Table S6D
Primers for competition assay	Wu et al.[13]	Table S6E
Recombinant DNA		
pCC1	Dr. Yonghui Zheng	N/A
pUC57	Dr. Yonghui Zheng	N/A
Software and Algorithms		
Perl	The Perl Foundation	https://www.perl.org
BioPerl PopGen library	Stajich[53]	https://bioperl.org
MUSCLE	Edgar[54]	http://www.drive5.com/muscle
SAMtools	Li[55]	http://www.htslib.org
R	The R Foundation for Statistical Computing	http://www.R-project.org

(*Continued on next page*)

Continued

REAGENT or RESOURCE	SOURCE	IDENTIFIER
R packages: gdata (version 2.18.0), ggplot2 (version 3.3.3), RColorBrewer (version 1.1.2), scales (version 1.1.1), ggsci (version 2.9), RColorBrewer (version 1.0.12), lme4 (version 1.1.27.1), cgam (version 1.16), gam (version 1.20), dplyr (version 1.0.6), trend (version 1.1.4), ggtree (version 3.0.2), ape (version 5.5), ape (version 5.5), treeio (version 1.16.1), patchwork (version 1.1.1), ggtreeExtra (version 1.1.3), ggnewscale (version 0.4.4)	The R Foundation for Statistical Computing	https://cran.r-project.org
FastTree	Price et al.[56]	http://microbesonline.org/fasttree
TreeCluster	Balaban et al.[57]	https://github.com/niemasd/TreeCluster
BEAST v1.10.4	Suchard et al.[58]	https://beast.community
Tracer	Rambaut et al.[59]	https://beast.community
BEAST2 PhyDyn	Bouckaert et al.[60] and Volz and Siveroni[61]	https://github.com/mrc-ide/PhyDyn
Other		
GISAID	Freunde von GISAID e.V.	https://www.gisaid.org
CoVdb	Zhu et al.[62]	http://covdb.popgenetics.net
The epidemic data of COVID-19	Global Change Data Lab	https://ourworldindata.org/covid-deaths
Nextstrain	Hadfield et al.[36]	https://nextstrain.org

RESOURCE AVAILABILITY

Lead contact

Further information and requests for resources and reagents should be directed to and will be fulfilled by the lead contact, Haibo Wu (hbwu023@cqu.edu.cn).

Materials availability

This study did not generate new unique reagents.

Data and code availability

All sequence data used in this study are available from GISAID (www.gisaid.org) and CoVdb (covdb.popgenetics.net). Clinical information (Clinical_Info.xls) obtained from GISAID, and unprocessed images of blots and gels have been deposited to Mendeley. Additional supplemental items are available from Mendeley data: https://doi.org/10.17632/bvrrsgm6c6.1.

EXPERIMENTAL MODEL AND SUBJECT DETAILS

SARS-CoV-2 virus

Wild type SARS-CoV-2 (USA_WA1/2020 SARS-CoV-2 sequence, GenBank: MT020880) virus (T492) was generated by using a reverse genetic method as previously described.[13,63,64] Briefly, the full-length cDNA was assembled by ligation (NEB Golden Gate Assembly Kit, New England Biolabs, MA, USA) of contiguous F1-F7 fragments spanning the entire genome of SARS-CoV-2. Then, full-length genomic RNA was collected by *in vitro* transcription (mMESSAGE mMACHINE T7 Transcription Kit, Thermo Fisher Scientific) and transfected into Vero E6 cells using Lipofectamine 3000 Transfection Reagent (Thermo Fisher Scientific). The SARS-CoV-2 virus was collected at 48 h post transfection, and viral titres were determined by plaque assays. The NSP4 T492I mutation (492I) was introduced to wild type virus by overlap-extension PCR as previously described.[13] The primers were listed in Table S6B. The sequences of all the seven fragments (F1-F7) were validated by sequencing and listed in Methods S1. The SARS-CoV-2 live virus related manipulations were performed under biosafety conditions in the BSL-3 facility at the Institut für Virologie, Freie Universität Berlin, Germany.

Cell lines

Human lung adenocarcinoma epithelial Calu-3 cells (HTB-55, ATCC, MD, USA) and African green monkey kidney epithelial Vero E6 cells (CRL-1586, ATCC) were maintained at 37 °C with 5% CO_2 in Dulbecco's modified Eagle's medium F12 (DMEM/F12, Gibco, CA, USA) supplemented with 10% FBS (Gibco). Cells were infected with a multiplicity of infection (MOI) of 0.01 at the indicated time points.

Hamster husbandry and infection

Six-week-old golden Syrian hamsters (Mesocricetus auratus) were obtained from Janvier Laboratories (Le Genest, St Isle, France) and kept in individually ventilated cages. The animals had unrestricted access to food and water and were allowed to acclimate to the conditions for 7 days prior to infection. For infection experiments, male and female hamsters were randomly assigned into different groups. Hamsters were anaesthetized by isoflurane and intranasally infected with 2×10^4 PFU virus. For the competition experiment, 12 hamsters received a 1:1 mixture of T492 and 492I virus. Hamsters were weighed and recorded daily. On day 3 and day 6 post infection, cohorts of 6 infected hamsters were anaesthetized with isoflurane, and nasal washes were collected with sterile PBS. The hamsters were then humanely euthanized immediately, and trachea and lung lobes were obtained as previously described.[38] This study was carried out in strict accordance with the Guidelines for the Care and Use of Animals of Chongqing University. All hamster operations were performed under isoflurane anaesthesia to minimize animal pain. The SARS-CoV-2 live virus infection experiments were performed under biosafety conditions in the BSL-3 facility at the Institut für Virologie, Freie Universität Berlin, Germany and performed in compliance with relevant institutional, national, and international guidelines for care and humane use of animal subjects.

Human airway tissue culture infection

Viral infection in a primary human airway tissue culture was performed as previously described.[13] Briefly, T492 or 492I virus was inoculated into a primary human airway tissue culture at a MOI of 5. After infection at 37 °C with 5% CO_2 for 2 h, the inoculum was removed and the culture was washed 3 times with PBS. Infected epithelial cells were maintained in the apical wells without any medium, and medium was provided to the culture through the basal wells. Infected cells were incubated at 37 °C with 5% CO_2. From day 1 to day 5 after infection, sterile PBS was added on the apical side of the tissue culture and incubate for 30 min at 37°C to elute released virus.

METHOD DETAILS

Statistics of SARS-CoV-2 mutations and VOCs

We used MN908947 strain collected in December 2019[1,62] as the reference. We performed pairwise alignments of the protein sequences of the reference strain and all sequenced strains, downloaded from GISAID (www.gisaid.org, updated at September 22, 2022). The alignments were used to identify the genomic position of the mutations. Based on the strain information of the phylogenetic tree provided by the Nextstrain database, we extracted the sample sequences of VOCs and built a library of the site substitutions of VOCs. The library was used to identify the attributes of all the sequenced strains. In the library, there were 288 substitution sites. We built shortened sequences containing these 288 sites using the alignments of all strains. The IF comparison was based on these shortened sequences.

We compared the IF of VOCs in T492 and 429I variants based on the 288 VOC site substitutions and all the shortened sequences. We calculated the changes of the 288 site substitutions between Delta T492 and Delta 492I variants in the days from April, 2021 to September, 2021 (a time window spanning the Delta era). For the 18 mutations differentiating Delta T492 and Delta 492I, we counted their IFs in Omicron variants in a ten-month time window after the onset of Omicron (from November, 2021 to Auguest, 2022).

We used a two-locus combination model to compare the growth rate of the 18 mutations within Delta strains. We took a comparison between a mutation A and mutation B as an example. Assuming that the mutant A1 of A has a higher growth rate than the wide-type A2 of A and the mutant B2 of B has an equal growth rate to the wild-type B2 of B, it is expected to observe a higher growth rate of the combination A1B1 than that of A2B1, a higher growth rate of A1B2 than that of A2B2, an equal growth rate between A1B1 and A1B2, and an equal growth rate between A2B1 and A2B2. In this case, the mutation in A increased in IF for 2 times (incCount=2) in the two associated combination comparisons (A1B1 vs A2B1 and A1B2 vs A2B2), and that in B had an incCount of 0. Moreover, the mutation in A should have a positive slope of the fitted line in average (aveSlope) in the two relevant combination comparisons, whereas the mutation in B should have an aveSlope near zero. The slope was calculated by the Python package ‘‘pymannkendall’’. A high positive slope indicates a rapid increasing trend and a negative slope indicates a decreasing trend. If extending to three or more mutation sites, e.g. A, B and C, and assuming that only the mutant in A has a growth advantage over the wide-type, we would expect that A has a higher incCount and a higher aveSlope of than other mutations. Thereafter, we calculated the incCount and aveSlope for each of the 18 mutations to predict the dominant mutation that differentiate Delta T492 and Delta 492I. We performed Mann-Kendall trend test (MK-test) and isotonic regression analysis (IR-test) to evaluate the significance of a growth. MK-test was performed by the R package ‘‘trend’’. IR-test was performed by the R package ‘‘cgam.’’[65] We calculated the trimmean as the aveSlope with a percent 0.1 based on the distribution of all calculated slope values. To ensure data sufficiency, we performed the evaluation in a long time window from April 2021 to September 2021. The IF was calculated based on the weekly running counts. The results showed that T492I had an incCount 34 in the 34 associated combination comparisons (binomial test, P-value 1.164e-10, Table S1). T492I had not only the highest incCount across the 18 mutations but also a higher aveSlope than other 17 mutations (Figure 1D; Table S1).

In the evaluation of the IF change of Delta T492I in Delta variants, we followed a reported approach[6] to compare the growth rates of different lineages. We wrote Perl scripts to evaluate the weekly running counts of Delta strains with and without T492I. In the evaluation of the changes of Delta 492I relative to Delta T492 variants, we performed Fisher’s exact test (Fisher-test) of the fraction of pairs of lineages on the onset, when a new variant was introduced, and at that date one month later. In the statistics in a country or regional subdivision level, we required counts above 10 at each time point for both the Delta T492 and Delta 492I sequences

to ensure the data adequacy. Due to empty or insufficient data for some countries/regional subdivisions at the early time points, we did not use April 1st, 2021 as the onset in the statistics in a country/regional subdivision level. Moreover, the real onsets of the spread of T492I in different countries may be different due to the geographic difference. Thus, we considered the first time point at which the count of Delta 492I was equal or less than the count of Delta T492 as the potential onset. We set the criteria to approximate the onset and to avoid mistakenly considering a time point far away post the real onset as a potential onset, which happens if there are insufficient or empty data in most early time points. We then compared the fraction of Delta 492I in all Delta variants in the potential onset and that in a second time point one month after the potential onset by Fisher-test. For an inclusion of more data, we allowed the time window to extend below 45 days if the data in the time points 30 to 44 days post the potential onset were missed. We built a maximum likelihood estimation line of the fraction trend and evaluated the trend by MK-test and IR-test. The fraction was calculated based on the weekly running counts of Delta T492 and Delta 492I. These evaluations were performed at three hierarchical geographic levels (world, country and region subdivision) and in a time window of three months after the global onset of Delta T492I (April 2021 to June 2021). Wilcoxon test and Fisher-test were performed by R.

Following a reported pipeline,[66] we evaluated the transmission advantages of Delta 492I variants compared to Delta T492 variants in the California State, USA. A phylogenetic tree was constructed using all SARS-CoV-2 sequences collected in the California State from April 2021 to September 2021. The phylogenetic clusters were identified by TreeCluster[57] with a parameter of -t 0.045. The clusters of Delta 492I were first detected later than clusters of Delta T492 (Figure 1I, P-value < 2.2e-16). The number of Delta 492I clusters (178) and Delta T492 clusters (173) were nearly equal, but the former were on average 191% larger than the latter (P-value = 0.004, Figure S1M). The sampling frequency of Delta 492I continued to increase in Delta variants (Figure S1N), and the earliest detected clusters were larger than those detected later (Figure S1O). In the evaluation of the growth rates by simulation models (Figures 1J, 1K, S1P, and S1Q), the simulations in a logistic growth coalescent model and in an exponential growth coalescent model were performed using an HYK substitution model, a strict clock type, an exponential prior distribution and a length of chains 10e7 by BEAST v1.10.4.[58] We used FastTree[56] (parameters, -boot 1000) to build the phylogenetic trees of Delta 492I and Delta T492 variants, respectively. The estimated mutation selection coefficient (s) of Delta 492I was 1.376 for the logistic growth coalescent model and 0.669 for the exponential growth coalescent model, assuming that the Delta T492 variants grow exponentially at a rate of r and the Delta 492I variants grow exponentially at a rate of r(1+s). Then, we performed phylodynamic inference of effective population size for time-scaled phylogenies by the R package Skygrowth[67] (parameters, res = 300 and tau0 = 0.1). Delta 492I variants showed a higher growth rate than Delta T492 variants with weak significance in a simulation with the skygrowth coalescent model (Figure 1L). The plotting and analysis of the simulation data were performed by R libraries ''gdata'' and ''ggplot2''.

The inference of relative fitness based on global vaccination coverage data

According to the theory of classical population genetics,[68] for two genotypes A and B in a population, the change in proportion (Δp) is:

$$\Delta p = \frac{p_t \lambda_A}{p_t \lambda_A + q_t \lambda_b} - p_t. \quad \text{(Equation 1)}$$

Here, p_t and q_t are the proportions of A and B in the population at the moment t, respectively. λ_A and λ_b are the absolute fitness of A and B, respectively. We manipulated the equation and obtained:

$$\frac{\lambda_A}{\lambda_B} = \frac{q_t(p_t + \Delta p)}{p_t(1 - p_t - \Delta p)}. \quad \text{(Equation 2)}$$

$\frac{\lambda_A}{\lambda_B}$ is the fitness of A relative to B at the moment. Based on Equation B, we inferred the fitness of Delta 492I relative to Delta T492 in a time interval of one-month after the onset of global spread of Delta T492I. We counted the weekly median of the relative fitness for each day. To ensure the data sufficiency in statistics, we filtered out the days without a >10 count both for Delta T492 and Delta 492I. We obtained the records of vaccination coverage (number of vaccinations per hundred people) from Our Word In Data (ourworldindata.org) and used R to perform a correlation test between the weekly median of the relative fitness and the global vaccination coverage. We also built a maximum likelihood estimation line of the fitness trend and evaluated the trend by MK-test and IR-test.[65] In a time window of one month after the onset of the global rise of Delta 492I (from April 1st, 2021 to April 30th, 2021), we observed a global increase in the predicted fitness of Delta 492I relative to that of Delta T492 (Figure S1R) and this increase was correlated with the increase of global VCs (Figure 1M). Due to insufficient data for most countries in the month after the global onset (Table S7), we did not perform correlation test at a country level.

The rise in the relative fitness of Delta T492I after the global onset and its correlation with the rise of VC indicates that T492I may function in resistance to neutralization and that global vaccination program may boost the rise of the VOCs with T492I. Following these, we evaluated whether an earlier vaccinated country would reach a high IF of Delta T492I at an earlier time to further assess the impact of T492I in terms of immune evasion capacity. Specifically, we evaluated the correlation between the date a country first reached a high IF of Delta 492I (e.g. 0.8) and the date the VC of the country increased to a certain degree (e.g. 0.5). For comparison purposes, we considered the date Jan 1st 2021 (near the onset of the global vaccination program) as the base point, and calculated the days between the base point and the date (time point 1) when a country first reached a high IF (fhIF, Delta T492I in all Delta variants) and the days between the base point and the date (time point 2) when a country first reached a VC of a certain degree (fVC). We also required a count of > 10 for both Delta T491 and Delta 492I at time point 1. For an identified time point 1 with a

high IF (e.g. 0.8), we required a >10 days of lower IF (e.g. <0.7) before the identified time point 1. This step was taken to avoid considering a day after the real first day when the country reached an fhIF, due to the empty or insufficient data in the days before the identified time point 1. We excluded the countries with an overly large land area or a gigantic population sizes, e.g. USA, Canada and India, in the correlation test. This is to diminish the bias caused by differences in population structure and population size. The traversal of fhIF is from 0.7 to 0.9 with a step 0.1. The traversal of fVC is from 0.1 to 0.5 with a step 0.05 according to the range of VC in 2021 (Figure S1S). The results show that most fVC-fhIF pairs have a positive correlation with a statistical significance (Binomial Test, P-value = 0.001431, Table S4).

Function prediction based on clinical data

We manually gathered clinical information of 115032 SARS-CoV-2 strains (Clinical_Info.xls in Mendeley Data) from GISAID. We retrieved the Delta T492 and Delta 492I strains collected from April 2021 to September 2021 (the time interval when T492 and 492I variants coexisted). Following the pipeline in our previous work,[8] we grouped this information into pairs of opposite patient statuses, according to a series of keywords (Table S8). We counted the number of variants with different patient statuses and tested the significance by using the chi-squared test.

Plaque assay, viral subgenomic RNA assay and genomic RNA assay

Plaque assays were performed as previously described.[13] Briefly, approximately 1×10^6 cells were seeded into 6-well plates, and cultured in 5% CO_2 at 37 °C for 12 h. T492 or 492I virus was serially diluted in DMEM containing 10% FBS, and 200 μL aliquots were supplemented into cells. Cells were co-incubated with virus and then supplemented with overlay medium that contains 1% SeaPlaque agarose (Lonza Bioscience, Basel, Switzerland). After 2 days of incubation, crystal violet (0.75% aqueous solution) was used to stain the plates, and plaques were calculated. Viral subgenomic RNA assay was performed with primers that target envelope protein (E) gene sequences.[13,69] Viral genomic RNA assay was performed with primers that target Orf1ab sequences as previously described.[13,70] Briefly, total RNA of infectious cell lysate was extracted using an RNeasy Mini Kit (QIAGEN, Hilden, Germany). RT-PCR was performed using an iTaq Universal SYBR Green One-Step Kit (Bio-Rad) and an ABI StepOnePlus PCR system (Thermo Fisher Scientific) according to the manufacturer's instructions. Primers used for viral sgRNA assay, genomic RNA assay and competition assay were listed in Tables S6C–S6E.

Competition assay

Competition assay was performed by RT-PCR with quantification of Sanger peak heights as previously described.[13] Briefly, a pair of common primers (Primers: SARS-CoV-2 9840F, 5'-AGTTGCGTAGTGATGTGC-3'; SARS-CoV-2 10296R, 5'- GAATGTCC AATAACCCTGA-3') was used to quantify the T492: 492I ratios. The 457 bp product was amplified using a SuperScript III One-Step RT–PCR kit (Thermo Fisher Scientific), followed by purification (GeneJET PCR Purification kit, Thermo Fisher Scientific) and Sanger sequencing (Primer for Sanger sequencing: 5'-AGTTGCGTAGTGATGTGC-3'). The electropherograms were scored by QSVanalyser software to determine the T492: 492I ratios.

Pathological examination and scoring

Pathological examination of hamster tissues was performed according to standard procedures. Briefly, hamsters were anaesthetized with isoflurane and tissues were harvested. Tissues were fixed in 10% formalin, and trimmed and embedded in paraffin for hematoxylin and eosin staining. The histopathology scoring of the infected hamsters was performed using a semi-quantitative pathology scoring system as previously described.[13] Five sections were collected from each hamster, and the scores of lung sections were summed to calculate a total score of each animal. All scoring was performed by the same operator to ensure consistency of scoring.

Pulmonary function test

Pulmonary function test was performed on hamsters infected with T492 or 492I virus and control group (naïve, 0 dpi) following a previous report with some modifications.[71,72] Briefly, hamsters were anaesthetized with a mixture of sodium pentobarbital (3 mg/100 g), α-chloralose (3.8 mg/100 g) and urethane (38 mg/100 g). Then hamsters were tracheostomized and cannulated with a 16GA catheter. Measurements of functional residual capacity, total lung capacity, vital capacity, residual volume, forced expiratory volume in in 100 ms were performed using previously described settings.[71,72]

Protein structure modeling and docking of NSP5 and substrates

Starting from the crystal structure of NSP4|5 peptidyl substrate (TSAVLQSGFR) (PDB: 7DVP).[73] The 3D structures of the T492 (QTSITSAVLQSGFR) and 492I (QISITSAVLQSGFR) substrates cleaved by SARS-CoV-2 NSP5 in this work were constructed using RosettaRemodel method.[74] The blueprint file was first obtained from the crystal structure of nsp4|5 peptidyl substrate. The structure was then locally refined by inserting four residues (QTSI for the T492 and QISI for 492I) on N-terminal, still using loop fragments. The sidechains of this newly built loop segment were designed automatically and generated 100 conformations. According to the score file, the first conformation was selected for the following computing. The 3D structure of SARS-CoV-2 NSP5 (PDB: 7DVP)[73] was retrieved from PDB database. Before docking, the mutation (H41A) in the crystal structure was mutated back to its native state using the mutagenesis tool in PyMOL. NSP5-substrate docking was performed by RosettaDock.[75] The structures of the two substrates and

NSP5 were firstly formed by the script of *clean_pdb.py*, and were refined by running relax protocol. Then, the structures of T492 and 492I substrates were manually docked to the relaxed structure of NSP5 using the nsp4|5 peptidyl substrate as a reference. The obtained model was further prepacked and used as a starting point for several rounds of local docking to generate 10,000 decoys by running docking with the Monte Carlo (MC) refinement algorithm. Finally, the energy funnel of each docking trajectory was depicted using the interface score (I_sc) and the interface root-mean-square deviation (I_rmsd).

Immunoprecipitation and immunoblot assay

Cell lysates were collected and lysed with RIPA Lysis Buffer (Merck Millipore, Darmstadt, Germany) containing protease inhibitor cocktail (Merck Millipore). Lysates were incubated with anti-His antibody (sc-8036, Santa Cruz Biotechnology, CA, USA) and Protein A-Agarose (Santa Cruz Biotechnology) overnight at 4°C. Precipitated protein complex was harvested and subjected to immunoblot assay. For immunoblot, samples were separated by sodium dodecyl sulfate polyacrylamide gel electrophoresis and transferred to polyvinylidene fluoride membranes (Merck Millipore). Blots were probed with anti-His (sc-8036, Santa Cruz Biotechnology), anti-Flag antibody (MA1-91878, Thermo Fisher Scientific) and visualized using a ChemiDoc imaging system (Bio-Rad, CA, USA).

Dual luciferase reporter assay

Dual luciferase reporter assay was performed using a dual luciferase reporter Assay System (Promega, WI, USA) according to the manufacturer's instructions. Cells were transfected with luciferase reporter plasmids, and internal control plasmid pRL-SV40 was cotransfected as an internal control. After 24 hours, cell lysates were harvested for dual luciferase detection using a VICTOR X5 Multilabel Plate Reader (PerkinElmer, Germany). Relative luciferase activity was measured by firefly luciferase luminescence divided by renilla luciferase luminescence.

Real-time qRT-PCR

Total RNA was isolated using an RNeasy Mini Kit (QIAGEN, Hilden, Germany). The mRNA was reverse-transcribed and quantified using an iTaq Universal SYBR Green One-Step Kit (Bio-Rad). qRT-PCR was performed on an ABI StepOnePlus PCR system (Thermo Fisher Scientific), and results were normalized to GAPDH mRNA levels. Data were analyzed using the $2^{-\Delta\Delta ct}$ method. The Primer sequences of IFN-β, IFN-λ, ISG56 and MX1 were provided in Table S6A.

Enzyme linked immunosorbent assay

Cell culture lysates were purified by centrifugation, and then assayed by enzyme linked immunosorbent assay as previously described.[13] Briefly, Calu-3 cells were infected with T492 or 492I virus at a MOI of 0.01. At 12, 24 and 48 h post infection, the cell lysates were harvested and subjected to standard procedures using specific NSP antibodies. Samples were probed with anti-NSP4 (SAB3501139, Merck Millipore), anti-NSP5 (SAB3501127), anti-NSP6 (SAB3501140), anti-NSP8 (SAB3501131), anti-NSP12 (NBP3-07963, Novus Biologicals, CO, USA), anti-NSP13 (NBP3-07055), anti-NSP15 (NBP3-11932), anti-NSP16 (A20283, ABclonal, MA, USA), anti-Nucleocapsid (MA5-42337, Thermo Fisher Scientific) and anti-Spike (MA5-42338) antibodies. The absorbance data were collected with a VICTOR X5 Multilabel Plate Reader (PerkinElmer, MA, USA). The concentration of each non-structural protein was calculated against a standard curve.

Proximity ligation assay

Proximity ligation assay was performed using a Duolink PLA Multicolor Probemaker kit (DUO96010, Sigma-Aldrich) according to the manufacturer's instructions. Briefly, Vero E6 cells were transfected with plasmids encoding Flag-tagged T492 or 492I substrates and then infected with SARS-CoV-2 virus. Cells were fixed with 4% PFA on slides and permeabilized with 0.2% Triton X-100. Oligo-conjugated anti-Flag and anti-NSP5 antibodies were diluted with Probemaker PLA Probe Diluent. After incubation, ligation, amplification and washing, the proximity of NSP5-substrates were determined by fluorescence intensity.

Isothermal titration calorimetry and Surface plasmon resonance

Isothermal titration calorimetry (ITC) and Surface plasmon resonance (SPR) were performed to determine the affinity of NSP5-substrates as previously described.[13] For ITC, purified proteins were transferred to buffer containing HEPES (20 mM, pH 7.5), NaCl (100 mM), and 2-mercaptoethanol (2 mM) by HiTrap desalting column (GE healthcare, GA, USA). Titrations were performed by using a Microcal PEAQ-ITC calorimeter (Malvern Panalytical, Malvern, UK) and data were analyzed using the PEAQ-ITC analysis software. For SPR, purified NSP5 protein (20 μg/mL) was coupled on a CM5 Chip (GE Healthcare, IL, USA) and different doses of T492 or 492I substrates were injected for dissociation analysis. Dissociation rate constants were determined using the steady state affinities vvobtained for each enzyme concentration.

Intracellular fluorescence resonance energy transfer

Schematic diagram of intracellular fluorescent resonance energy transfer assay was shown in Figure S3 following a previous report with modifications.[76] HEK-293T cells were transfected with CMV-3×492I(TAG)-NSP5-YFP or CMV-3×T492(TAG)-NSP5-YFP plasmid, and then treated with 50 μM ANAP. After 18 hours, cells were transfected with different dose (0.5, 1.0 and 2.5 μg,

respectively) of 3×T492 or 3×492I plasmid. A fluorescent amino acid ANAP was incorporated into the T492 or 492I substrate. The fluorescence of ANAP-substrate was detected with excitation at 405 nm, and the fluorescence of YFP-NSP5 was detected with excitation at 488 nm.

Statistical Analysis

Sample size was based on empirical data from pilot experiments. The investigators were blinded during data collection and analysis. A value of $P < 0.05$ was considered significant. Specific details of statistical analysis are presented above or in associated figure legends.